Chapter 1
Mechanics and Modeling of Chip Formation in Machining of MMC

Yung C. Shin and Chinmaya Dandekar

Abstract Metal matrix composites (MMCs) offer high strength-to-weight ratio, high stiffness and good damage resistance over a wide range of operating conditions, making them an attractive option in replacing conventional materials for many engineering applications. Typically the metal matrix materials of MMCs are aluminum alloys, titanium alloys, copper alloys and magnesium alloys, while the reinforcement materials are silicon carbide, aluminum oxide, boron carbide, graphite etc. in the form of fibers, whiskers and particles. This chapter covers the mechanics of chip formation during machining of MMCs and various modeling techniques. Especially, modeling techniques dealing with cutting force, chip morphology, temperature and subsurface damage are covered.

1.1 Introduction

Metal matrix composites (MMCs) offer high strength to weight ratio, high stiffness and good damage resistance over a wide range of operating conditions, making them an attractive option in replacing conventional materials for many engineering applications. Typically the metal matrix materials of MMCs are aluminum alloys, titanium alloys, copper alloys and magnesium alloys, while the reinforcement materials are silicon carbide, aluminum oxide, boron carbide, graphite etc. in the form of fibers, whiskers and particles. Probably the single most important difference between fiber reinforced and particulate composites or conventional metallic materials is the directionality of properties. Particulate composites and conventional metallic materials are isotropic, while the fiber reinforced composites are generally anisotropic. Particulate reinforced composites offer higher ductility and

---

Y. C. Shin (✉) · C. Dandekar
School of Mechanical Engineering, Purdue University, West Lafayette, IN, USA
e-mail: shin@purdue.edu

J. P. Davim (ed.), *Machining of Metal Matrix Composites*,
DOI: 10.1007/978-0-85729-938-3_1, © Springer-Verlag London Limited 2012

their isotropic nature as compared to fiber reinforced composites makes them an attractive alternative.

Machining of particulate reinforced MMC has been extensively studied experimentally in the past, while studies on the machining of fiber-reinforced MMCs is limited. MMCs are shown to cause excessive tool wear, which in turn induces such damage phenomena as fiber pullout, particle fracture, delamination and debonding at the fiber or particle and matrix interface. The parameters that are the major contributors to the machinability of these composites are the reinforcement type and orientation, tool type and geometry and the machining parameters. Although MMCs are generally processed near-net shape, subsequent machining operations are inevitable.

The methods used in studying the machining of composites have been diverse, and the investigations can be generally divided into three categories: experimental studies focusing on the macro/microscopic machinability of composites, simple modeling using conventional cutting mechanics, and numerical simulations that treat a composite as a macroscopically anisotropic material or concentrate on the reinforcement–matrix interaction microscopically. The macroscopic models normally ignore many fundamental characteristics of composites subjected to cutting and usually cannot be well integrated with the cutting mechanics, while those focusing on the micro-effects, including the analysis using the finite element method, are tedious to implement. A sensible way seems to combine the merits of these methods to develop realistic models that not only depict the material removal mechanisms in cutting, but also provide simple, analytical solutions for applications.

This chapter deals with understanding the mechanics of chip formation in machining of MMC. Optimization of machining parameters to achieve a better surface finish, reduced damage and maximum tool life is highly desirable. Understanding the mechanics of cutting would assist in selecting the optimum machining parameters so as to improve the machinability of these composites.

1.2 Machining of Particulate Reinforced Metal Matrix Composites

Most of the research related to machining of particulate reinforced MMC is attributed to turning and has been extensively studied experimentally in the past to assess the cutting forces, cutting temperature, the attendant tool wear, surface roughness and sub-surface damage. From the available literature on machining of MMCs it is obvious that the reinforcement material, type of reinforcement (particle or whisker), volume fraction of the reinforcement, and matrix properties as well as the distribution of these particles in the matrix are the factors that affect the overall machinability of these composites. The most commonly used tool material is polycrystalline diamond (PCD) [1–7], although cubic boron nitride (CBN), alumina, silicon nitride and tungsten carbide (WC) tooling are also used as cutting materials. Cutting speed, feed and depth of cut in machining of particulate MMCs have a similar effect on tool life and surface finish to that of machining metals although some differences are noticeable due to the ceramic particles. The ceramic-reinforced particles tend to dislodge from the matrix and roll in front of the cutting tool, thereby plowing through the machined surface and generating grooves on it [8, 9].

1.2.1 Effect of Cutting Speed

In most cases, cutting speed does not significantly influence the cutting forces [10]. There are some contradictory reports on the effect of cutting speed on the cutting forces. During machining of MMCs a built-up edge (BUE) has been observed by many researchers while machining these composites at low cutting speeds [9, 11, 12]. Due to the BUE the cutting force at low cutting speeds is lower than the cutting force observed at higher cutting speeds. This phenomenon can be attributed to either higher tool wear at high cutting speeds or the presence of BUE. The presence of a BUE increases the actual rake angle of the tool resulting in a lower cutting force. There are some studies which have shown a decrease in the cutting forces with an increase in the cutting speed [13, 14]. In the study conducted by Manna and Bhattacharya [14], the influence of the cutting speed on the feed force and cutting force during turning of an Al/SiC composite was measured. The experimental results showed that the feed force and the cutting force decreased with an increase in the cutting speed.

The tool life decreases while the surface finish improves only slightly with an increase in cutting speed, since the tool temperature increases with cutting speed, thereby softening the tool material and consequently accelerating the diffusion wear [3, 15, 16]. Overall, the variation of surface roughness with cutting speed is not significant as the surface roughness is dominated by the size of reinforcement and the feed [3, 16, 17]. In terms of tool life, Manna and Bhattacharya [9, 11] conducted studies using carbide tooling for machining of an Al/SiC composite and observed that the flank wear increased 2.5–3 times for an increase in cutting speed from 60 to 180 m/min. Another observation of flank wear variation with cutting speed is the very rapid increase in flank wear at cutting speeds above 100 m/min and hence cutting speed range of 60–100 m/min was suggested for machining of these composites. Ozben et al. [12] and Joshi et al. [18] both machined an aluminum matrix reinforced with SiC particles and observed that the cutting speed was one of the dominant factors in limiting the machinability of the composite.

1.2.2 Effect of Feed

Feed has a significant effect on the cutting forces in that the cutting forces rise considerably with an increase in the feed [10, 19]. There are many force prediction models available in the literature for machining of MMCs. For instance, Kishawy et al. [20] developed an energy-based analytical model to predict the forces in orthogonal cutting of an MMC using a ceramic tool at a low cutting speed, while Pramanik et al. [19] developed a mechanics-based model for prediction of the cutting forces based on the mechanisms of chip formation, and the presence of the matrix and particle. Feed, on the other hand, negatively influences the surface roughness, where the surface finish deteriorates with an increase in feed [3, 21]. Furthermore feed has the largest effect on the damage observed in the sub-surface [8, 22, 23], where larger feed results in more damage and also greater damage depth into the material. El-Gallab and Sklad [8, 23] concluded that the failure in the composite initiates along the voids generated around the SiC particles due to the high cutting forces observed at higher feeds. The voids join up to form micro-cracks and subsequent fracture along the shear band. On the other hand feed tends to have less influence on the tool wear. A high feed can reduce the tool-wear rate due to the improvement in the conduction of heat from the cutting zone to the workpiece [15]. Feed increases the flank wear but only marginally as compared to cutting speed. At a cutting speed of 60 m/min increasing the feed three folds increased the flank wear 1.6 times, while increasing the speed three folds at a feed of 0.35 mm/rev the flank wear increased three times [9, 24].

1.2.3 Effect of Depth of Cut

Depth of cut has a negative effect on the surface finish and the sub-surface damage. An increase in depth of cut decreases the quality of the surface finish and the sub-surface damage. Chambers [25] conducted a study on machining of a 15% by volume fraction of SiC in A356 aluminum alloy and concluded that the depth of cut did not significantly alter the tool life, with tool life decreasing with an increase in the depth of cut. Although the effect of depth of cut on tool wear is not significant, it has a stronger effect on the tool wear as compared to the feed as shown in machining of an Al/SiCp/15% composite with uncoated tungsten carbide tools [9, 15]. Additionally, an increase in the depth of cut increases the machining forces during the machining of MMCs.

1.2.4 Effect of the Reinforcement

Absent in machining of homogenous materials, the presence of the reinforcement affects the machinability of composites substantially. The hard ceramic particles in the matrix cause numerous problems, especially the excessive tool wear. The size and the percentage volume fraction of the reinforcement play a significant role on the machinability of composites. An expected result is the progression of tool wear and surface finish is highly dependent on the average size and volume fraction of the particles. Ciftci et al. [26] machined an Al/SiCp composite with SiC particle size of 30, 45 and 110 μm and a reinforcement of 16% volume using both coated and uncoated carbide tools. The authors reported that the tool wear and the surface finish are negatively affected by the particle size. This observation was further substantiated by Kannan et al. [15] while machining a composite with 10% by volume fraction of alumina particles in an Al 6061 matrix, with average particle size of 9.5, 17, 20 and 25 μm. An increase in particle volume fraction also results in increased tool wear and subsequently affects the surface finish of the machined workpiece. Higher tool wear is the result of the hard ceramic particles seen at a higher frequency by the cutting tool [3, 15, 26].

Similarly, Ozben et al. [12] machined an aluminum matrix reinforced with SiC particles in 5, 10 and 15% by volume fraction and observed that the cutting speed and percentage volume fraction of the particles were the dominant factors in limiting the machinability of the composite. Joshi et al. [18] studied the effect of feed (0.084–0.17 mm/rev), cutting speed (22–88 m/min), tool inclination angle (15 and 45°) and percentage volume fraction of SiC particles in aluminum (10 and 30%) on machining of the MMC with a carbide tool and arrived at an empirical relationship between flank wear and cutting time as a function of the aforementioned parameters. The authors concluded that the cutting speed and the percentage volume fraction of the particles had the most significant effect on the tool life.

1.2.5 Tooling

PCD diamond tools are the most preferred, while carbide tools are preferred over ceramic tools [1–4, 6, 7, 27]. In case of carbide tooling low-cutting speeds and high-feed rates are utilized to maximize the tool life [15, 28]. High tool wear observed while machining of these composites is generally associated with carbide tooling. At higher cutting speeds (>350 m/min), the carbide tool demonstrates catastrophic failure and hence in the literature cutting speed is generally limited up to 300 m/min [9, 11, 12, 18, 25, 29–31]. In other tool materials, Tomac and Tonnessen [28] compared the performance of chemical vapor deposition (CVD) coatings of TiN, TiCN and Al_2O_3 and concluded that the inserts with TiN coating performed the best in maximizing the tool life. To improve the tool life in carbide tools, Manna and Bhattacharya [9] machined at cutting conditions that sustained a stable built-up edge (BUE) so as to protect the cutting tool. To minimize the surface roughness and sub-surface damage PCD tools are preferred since the wear rate associated with them is the lowest among available tool materials. Although PCD tools are used for machining Al/SiC composites, the high cost associated with them limits their use [3–5, 16, 27].

1.3 Machining of Fiber Reinforced Metal Matrix Composites

Ceramic fiber reinforced MMC have seldom been machined with conventional machining methods. The fibers can be either short or long and continuous as governed by their application. The reinforcements enhance the properties of the metal matrix by increasing the fracture toughness, resistance to high temperatures, strength and damage tolerance. The composite properties are highly dependent on the type of reinforcement as the mode of failure will differ. Continuous fiber reinforcements are stiffer than particulate or whisker reinforcements [32] in the fiber direction. Similar to machining of monolithic ceramics, continuous fiber MMCs are generally not machined using conventional machining techniques like milling and turning due to the hardness of the constituent fibers. Fibers present in the metal matrix pose another problem for machining of MMCs as any fiber breakage or pullout causes a reduction in the material properties. Furthermore silicon carbide (SiC) fibers and boron nitride interface are susceptible to oxidation and hence care must be taken during machining. Komanduri [33] reported that in machining of a glass reinforced with continuous fibers of silicon carbide no cutting tool material could achieve respectable tool life. In conventional machining tests, Varadarajan et al. [34] studied the machinability characteristics of a low-volume fraction (25%), random aluminosilicate fiber reinforced aluminum composite with two tool materials; coated carbides and polycrystalline cubic boron nitride (PCBN). The results indicated that PCBN tools outperformed coated carbides in terms of tool wear and surface finish. In another study on machining of short-fiber reinforced metal matrix composite, Weinert and Lange [35] assessed the machinability of a 20% by volume fraction of Al_2O_3 fiber in a magnesium alloy matrix, wherein milling was carried out with a PCD tool, and the authors suggested the use of moderate cutting speeds and high feed to offset the high tool wear. Machining experiments were conducted by Dandekar and Shin [36] on an Al-2%Cu aluminum matrix composite reinforced with 62% by volume fraction alumina fibers (Al-2%Cu/Al_2O_3). The cutting speed was 30 m/min with feed of 0.02 mm/rev and 0.5 mm depth of cut. The cutting tool material is a PCD tool with a tool rake angle of 5°. Damage in the composite was measured and it was characterized in this case through excessive fiber breakage below the cutting plane. Due to the brittle nature of the alumina fiber there was observable damage below the cutting plane. Damage was observed in the form of debonding between the fiber and the matrix, microcracking of fibers and fiber pullout.

The excessive tool wear and damage associated with machining of long-fiber reinforced MMC results in the process being uneconomical. It is clear that the presence of reinforcement makes MMCs different from monolithic materials due to incorporation of its superior physical properties. In addition, the amount and type of reinforcement introduce different properties in the strength and toughness of composites. Higher fiber/particulate reinforcement results in a reduction in the ductility of MMCs, causing harsh machining conditions.

1.4 Mechanics of Machining MMC’s

Machining of MMCs can be classified into two major categories: a particulate reinforced and (b) fiber reinforced. Depending on the type of reinforcement, the cutting mechanics differ considerably. It is therefore clear that the tool–

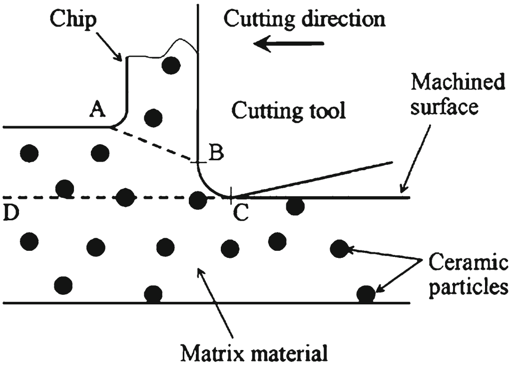

Fig. 1.1 Cutting of an MMC (*source*: Zhang [41], with permission from Elsevier)

reinforcement–matrix interactions play a significant role in the machinability of MMC's and affect the surface roughness, cutting forces, tool wear and the sub-surface damage.

1.4.1 Analytical Machining Model to Predict Cutting Forces

In terms of analytical modeling to predict the cutting forces, a number of authors have tackled this problem [19, 20, 37]. Kishawy et al. [20] were among the first to propose an analytical model for prediction of cutting forces. The model is an energy-based method, where the energy is estimated based on the deformation of the primary and secondary zones and the fracture and displacement of the reinforcement. Although the model was successful in predicting the cutting forces, it was based on two assumptions: the energy in the secondary deformation zone was one-third of that of the primary deformation zone and the initial and final crack lengths of the ceramic particles were 1 μm. The first assumption was based on the results obtained for machining of steel while no justification was made for the second assumption. Pramanik et al. [19] and Davim [37] both developed the cutting force model based on Merchant's orthogonal machining model. The major difference in their models is that Pramanik et al. [19] explicitly treat the effects of particles in their model as opposed to treating the composite as an equivalent homogenous material in the model proposed by Davim [37].

In the model developed by Pramanik et al. [19], the cutting force was predicted by splitting the total force into (a) the chip formation force, (b) the plowing force and (c) the particle fracture force. The chip formation force was obtained using Merchant theory [38], while the plowing and particle fracture forces were obtained with the aid of the slip line field theory of plasticity [39] and the Griffith theory of fracture respectively. Figure 1.1 shows a schematic of orthogonal machining of a particulate MMCs. According to Pramanik et al. [19] the mechanism of chip formation is due to shearing along the shear plane AB marked in Fig. 1.1. This assumption allows the chip formation mechanism to be similar to orthogonal machining of a monolithic material with a sharp tool. The plowing force (plastic zone with no chip) is due to the material deformation and the particle displacement, a result of the tool edge radius, as shown as BC in Fig. 1.1. Finally the force due to the particle fracture is accounted for along the line CD. This assumption is based on experimental observations of Yan and Zhang [40].

The total cutting force is therefore assumed to be a superposition of the cutting forces due to the individual contributions from chip formation, plowing and particle fracture as shown in Eqs. 1.1 and 1.2 for the total force in the cutting direction (F_C) and the thrust direction (F_T), respectively as:

$$F_C = F_{Cc} + F_{Cp} + F_{Cf} \tag{1.1}$$

$$F_T = F_{Tc} + F_{Tp} + F_{Tf} \tag{1.2}$$

where F_{Cc} and F_{Tc} are the forces due to chip formation, F_{Cp} and F_{Tp} are the forces due to plowing and F_{Cf} and F_{Tf} are the forces due to particle fracture. The force components for them are obtained as shown in Eqs. 1.3–1.7.

$$F_{Cc} = \tau_s A_c \frac{\cos(\beta - \gamma)}{\sin\phi \cos(\phi + \beta - \gamma)} \tag{1.3}$$

$$F_{Tc} = \tau_s A_c \frac{\sin(\beta - \gamma)}{\sin\phi \cos(\phi + \beta - \gamma)} \tag{1.4}$$

$$F_{Cp} = \tau_{sm} l r_n \tan\left(\frac{\pi}{4} + \frac{\gamma}{2}\right) \tag{1.5}$$

$$F_{Tp} = \tau_{sm} l r_n \left(1 + \frac{\pi}{2}\right) \tan\left(\frac{\pi}{4} + \frac{\gamma}{2}\right) \tag{1.6}$$

$$F_{Cf} = F_{Tf} = \left(\frac{\mu_g l}{L}\right) \tan\delta \tag{1.7}$$

where A_c is the cross-sectional area of the cut, τ_s is the shear strength of the MMC, τ_{sm} is the shear strength of the matrix, r_n is the edge radius, β is the angle of friction, γ is the tool rake angle, ϕ is the shear angle, δ is the resultant cutting force angel, L is the cutting distance, μ_g is the average fracture energy per unit cutting edge length and l is the active cutting edge length. The shear angle and the average cutting edge length are calculated by Eqs. 1.8 and 1.9, respectively.

$$\tan\phi = \frac{r_c \cos\gamma}{(1 - r_c \sin\gamma)} \tag{1.8}$$

where r_c is the chip thickness ratio.

$$l = r_\varepsilon \left[\kappa_r + \arcsin\left(\frac{f}{2r_\varepsilon}\right)\right] + \frac{d - r_\varepsilon[1 - \cos(\kappa_r)]}{\sin(\kappa_r)} \tag{1.9}$$

where r_ε is the tool nose radius, κ_r is the approach angle, f is the feed and d the depth of cut.

Table 1.1 Cutting conditions for particulate MMC

Parameters	Chambers [25]	Davim [21]	Pramanik et al. [19]
Tool material	PCD	PCD	PCD
Nose radius (mm)	1.6	0.8	0.4
Rake angle (deg)	0	0	5
Approach angle (deg)	85	85	90
Cutting speed (m/min)	50–300	250–700	100–800
Feed (mm/rev)	0.2	0.1	0.1–0.25
Depth of cut (mm)	1	1	0.25–1.5
Workpiece	A356-15% SiC	A356-20% SiC-T6	A6061-20% SiC
Yield strength of matrix (MPa)	138	138	110
Average particle diameter (micron)	22.5	20	12

The authors validated the analytical model with their experimental results as well as those published in the literature showing that the theoretical model captured the major mechanisms of machining MMCs and the predicted cutting forces compared well with experimental results. Table 1.1 summarizes the cutting conditions used in the validation of the theoretical model with experimental results published in the literature. The theoretically predicted cutting forces are within 6–11% of the experimental measurements done by Chambers [25] and Davim [21]. Additionally the model developed by Pramanik et al. [19] is compared to the cutting force predictions based on the model by Kishawy et al. [20].

Figure 1.2 compares the predicted and experimental forces with varying feed, where the cutting and thrust forces increase more or less linearly with an increase in the feed. The cutting and thrust forces predicted from the model developed by Pramanik et al. [19] compare better with experimental results as opposed to the predictions made by the Kishawy et al. [20] model. The trend is maintained in the comparison of cutting forces with varying depth of cut (Fig. 1.3). On the other hand the cutting forces decrease approximately linearly with an increase in the cutting speed as shown in Fig. 1.4. Once more the predictions obtained from Pramanik et al. [19] are closer to experimental results than the predictions obtained from Kishawy et al. [20].

Although the theoretical force model predicts cutting forces accurately it still is an approximation of turning into an orthogonal cutting model. This limits the information supplied by the predictive model and hence numerical techniques such as finite element methods have become popular in carrying out machining simulations as will be discussed later in the chapter.

1.4.2 Cutting Temperatures in Machining of MMC

During cutting, high temperatures are generated in the region of the tool cutting edge as a form of cutting energy dissipation. These temperatures have a controlling influence on the rate of wear of the cutting tool and on the friction between the chip and tool, and they can significantly affect the functional performance of a

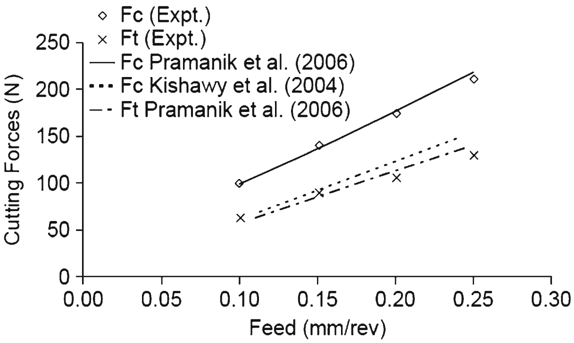

Fig. 1.2 Comparison of predicted and experimental forces with varying feed

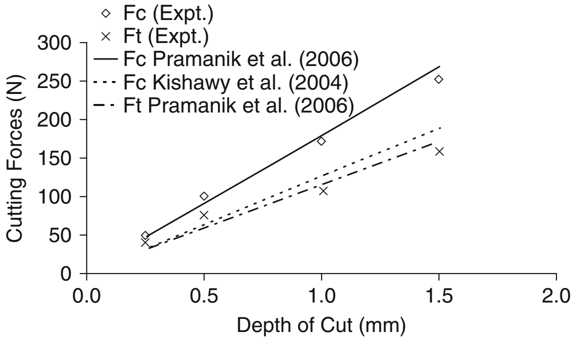

Fig. 1.3 Comparison of predicted and experimental forces with varying depth of cut

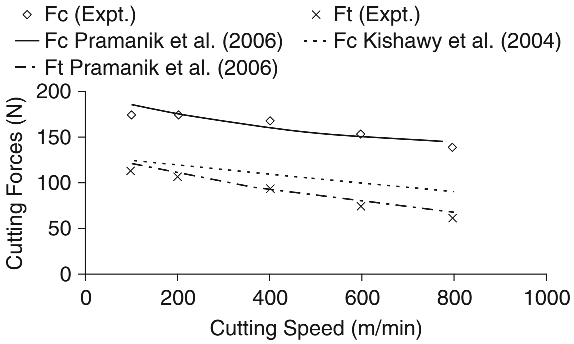

Fig. 1.4 Comparison of predicted and experimental forces with varying cutting speed

machined part due to residual stresses or thermal distortion. Therefore considerable attention has been paid to the measurement and prediction of the temperatures in the tool, chip and workpiece in metal cutting.

Analytical models to exclusively predict cutting temperatures in machining of MMCs do not exist. Therefore many of the studies consider the material to be an equivalent homogenous material and utilize analytical models developed for metal cutting. In metal cutting the material is subjected to extremely high strains and predominantly plastic deformation. By assuming the elastic deformation to only be a very small portion of the total deformation, it is assumed that all the energy required in cutting is converted into heat.

Table 1.2 Values of Γ for machining of an aluminum alloy reinforced by SiC particles

Cutting speed (m/min)	Feed (mm/rev)	Γ
60	0.1	0.52
60	0.3	0.28
180	0.1	0.25
180	0.3	0.17

Workpiece: A359/SiC/20p; tool: CVD coated WC insert; nose radius: 0.8 mm; rake angle: 0°; relief angle: 11°; lead angle: 0°
Source: Liu and Chou [43]

In cutting there are two major regions of plastic deformation responsible for the conversion of energy into heat: the shear zone, or primary deformation zone, and the second deformation zone along the tool–chip contact. There is an additional heat source when the tool has flank wear. This third heat source is a result of the friction between the tool flank face and the workpiece. If the tool is not severely worn the heat generated due to the rubbing of the flank face is negligible and can be neglected. Details on the derivation of the analytical models for calculating the temperatures in metal cutting can be obtained from Boothroyd and Knight [42].

The first heat source is the heat generated due to the shearing of the chip. The energy liberated due to chip shearing (P_s) is given by Eq. 1.10.

$$P_s = F_s v_s \tag{1.10}$$

where F_s is the shear force and v_s is the chip velocity along the shear plane. Using Merchant's theory the shear force is calculated by Eq. 1.11.

$$F_s = F_C \cos\phi - F_T \sin\phi \tag{1.11}$$

where F_C and F_T are the cutting and thrust force and ϕ is the angle of the shear plane given by Eq. 1.8.

A fraction, Γ, of the heat generated in the shear zone is conducted into the workpiece, while the remainder is transported with the chip and is estimated to be approximately 80% of the total heat generated in the shear zone [42]. A similar approximation was used by El-Gallab and Sklad [6] in their study of machining of an aluminum matrix with a 20% by volume fraction reinforcement of SiC particles. Values of Γ for an aluminum alloy (A359) reinforced with 20% by volume fraction of SiC composite were numerically estimated by Liu and Chou [43] and are summarized in Table 1.2. The value of Γ depends on the workpiece material, tool/workpiece combination and the cutting conditions employed; hence care must be taken in using the values shown in Table 1.2.

According to Weiner's relationship [44], the shear plane temperature (θ_s) is evaluated by Eq. 1.12.

$$\theta_s = \frac{(1-\Gamma)P_s}{(\rho c v_s t_o a_w)} \tag{1.12}$$

where ρc is the volumetric specific heat, t_o is the uncut chip thickness, a_w is the width of cut and Γ is the portion of the heat source conducted back to the workpiece.

Compared with the experimental data obtained by El-Gallab and Sklad [6], the theory provides slightly underestimated results. In the theory a plane heat source was assumed and that heat can only flow into the workpiece by conduction. In reality heat is generated over a wide zone, part of which extends into the workpiece. The effect of this wide heat generation zone becomes increasingly important at high speeds and feeds, therefore the deviation between theoretical and experimental data could be explained.

The second heat source is the heat generated along the tool-chip interface due to friction. The energy liberated due to friction is given by Eq. 1.13.

$$P_f = F_C \mu v \tag{1.13}$$

where F_C is the cutting force which can be calculated using Eq. 1.1, μ is the coefficient of friction and v is the chip velocity which can be given by Eq. 1.14.

$$v = r v_c \tag{1.14}$$

where r is the chip ratio and the v_c is the cutting speed.

The maximum temperature in the chip takes place at the exit from the secondary deformation zone and is given by Eq. 1.15.

$$\theta_{\max} = \theta_o + \theta_s + \theta_m \tag{1.15}$$

where θ_o = initial workpiece temperature, θ_s = temperature increase due to the material passing through the primary deformation zone and θ_m = temperature increase as material passes through the secondary deformation zone. The following solution was obtained by Rapier [45] for θ_m as shown in Eq. 1.16.

$$\theta_m = 1.13\theta_f \sqrt{\frac{R}{l_o}} \tag{1.16}$$

where l_o = ratio of the heat source length to the chip thickness l_f/t_c. R is a dimensionless number given by $\rho c V a/k$ and known as the thermal number, with ρ being the density (kg/m^3), k the thermal conductivity (J/(s(m)K)), c the specific heat capacity (J/(kg K)), V the velocity of the material (m/s) and a the linear dimension which for single point turning is typically the width of cut.

θ_f is the average temperature increase of the chip resulting from the secondary deformation as given by Eq. 1.17.

$$\theta_f = \frac{P_f}{\rho c V t_o a_w} \tag{1.17}$$

A comparison of calculated values of Eq. 1.17 by Rapier [45] with experimental data showed that his theory considerably overestimated θ_m. This could be explained by the fact that the friction-deformation zone, instead of being planar, has a finite width in the analytical model. Once again compared with experimental data obtained by El-Gallab and Sklad [6], the theory overestimates the temperature measurements along the tool rake face. Therefore, from analytical models it is clear that the cutting temperatures deviate from experimental measurements.

Numerical methods such as finite-element models are therefore attractive for studying the cutting temperatures in machining of MMC.

1.4.3 Chip Formation of Particulate MMC Cutting

Chip formation involves the plastic deformation of the shear zone in machining. Traditionally, in metal cutting the shear zone can be analyzed based on the thin-plane model or the thick-plane model. At higher cutting speeds the shear zone approximates to the thin-plane model which allows for easy determination of the shear zone angle. In practice MMCs are machined at relatively high-cutting speeds and therefore the approximation to a thin-plane model is representative of the cutting process. However, the formation of chips cannot be only related to the nature of the shear zone but is also related to the material properties, microstructure and instabilities in the cutting process. The types of chips formed in turning are highly dependent on the cutting conditions. Broadly, the types of chips are classified as (a) Continuous, (b) Built-up Edge, (c) Serrated and (d) Discontinuous and shown schematically and with micrographs in Fig. 1.5.

Typically continuous chips are usually formed when machining at higher cutting speeds and/or machining with cutting tools with a high-rake angle. The deformation of the chip occurs primarily in the primary shear zone marked in Fig. 1.5a with some deformation occurring along the secondary shear zone shown in Fig. 1.5b. Continuous chips are generally not desirable as they tend to get tangled up causing unnecessary delays in machining operations. Chips with built-up edges are generally formed when machining at lower cutting speeds. This phenomenon has been widely observed when machining aluminum matrix MMCs. The built-up edge (Fig. 1.5c) consists of layers of materials from the workpiece that is gradually deposited on the tool. As the material builds up, the BUE becomes larger and subsequently becomes unstable and breaks off. Some of the broken BUE is carried away by the chip while the remaining BUE adheres to the machined workpiece. The BUE is to a certain extent undesirable since it is one of the reasons for a poor surface finish. On the other hand a thin stable BUE is desirable as it is found to protect the tool surface thereby prolonging the tool life. Serrated chips shown in Fig. 1.5d are semi-continuous chips with zones of low-and high-shear strain. The chips demonstrate a sawtooth like pattern and are generally associated with machining of low-thermal conductivity materials like titanium. Discontinuous chips associated with machining of brittle materials, thermosetting polymer composites, MMC at very low- or very high-cutting speeds are shown in Fig. 1.5e. Impurities and hard particles (reinforcements) act as nucleation sites for cracks and therefore result in discontinuous chips.

In machining of MMCs, the most common types of chips are serrated and discontinuous chips with continuous chips formed under certain limited cutting conditions. Lin et al. [3] observed sawtooth-type chips that are most commonly observed while machining titanium alloy. The chip formation mechanism is

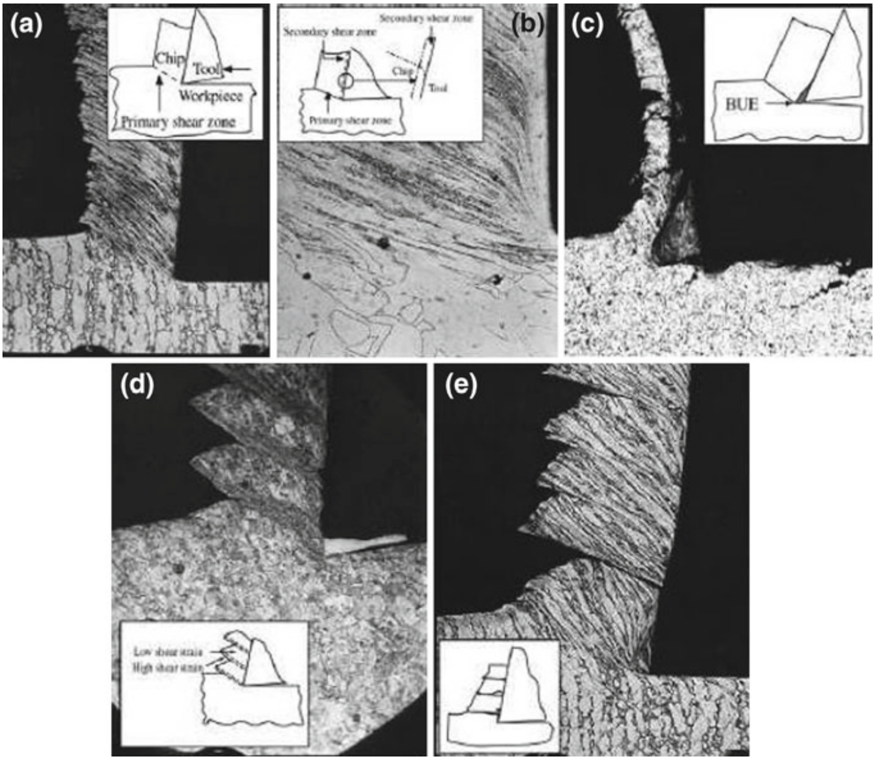

Fig. 1.5 Basic types of chips produced in metal cutting. **a** Continuous chip with narrow, straight primary shear zone. **b** Secondary shear zone at the chip-tool interface. **c** Continuous chip with built-up edge. **d** Segmented or nonhomogenous chip. **e** Discontinuous chip (*source*: S. Kalpakjian [46])

accompanied by a severe plastic deformation of the shear zone. The addition of silicon carbide in the aluminum alloy reduces the ductility of the material contributing to the segmental chip. The chip formation mechanism involves the initiation of cracks, void formation due to the separation of the particles and matrix, subsequent coalescence of the voids, propagation along the shear zone and fracture and sliding of the material to form the semi-continuous chips. Additional tests conducted on aluminum alloy MMCs showed that sharp tools produced continuous chips, while worn tools, higher feed or depth of cut resulted in semi-continuous chips [3, 4, 47]. Researchers have also found similarities in the chip formation mechanism of MMCs to that of conventional monolithic materials. Flow lines associated with particles in the MMCs are similar to the flow lines due to the deformation of grain boundaries of aluminum, titanium and steel [48–50] with the particles aligned along the shear plane in the chip root region. On the other hand the presence of displaced and fractures particles play an important role in machining of MMCs [4, 19]. Therefore the chip formation mechanism is highly

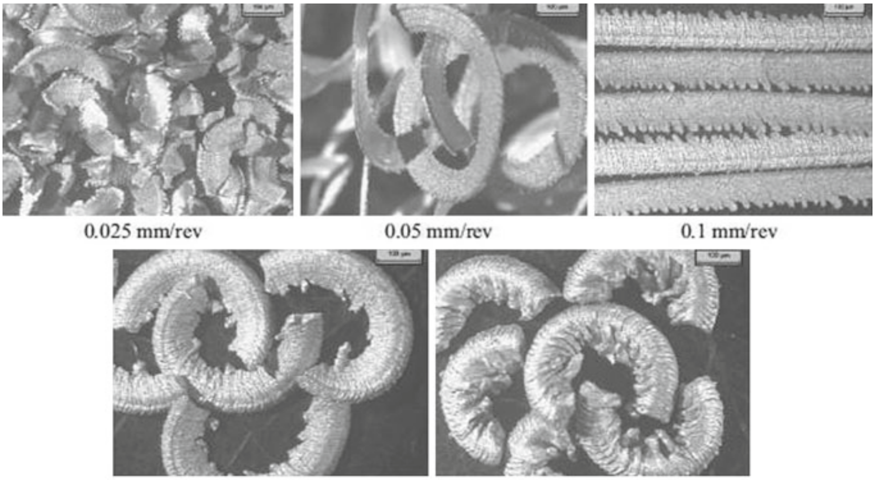

0.025 mm/rev 0.05 mm/rev 0.1 mm/rev

0.2 mm/rev 0.4 mm/rev

Fig. 1.6 Chip shapes of the MMC at different feeds (at speed of 400 m/min and depth of cut 1 mm) (*source*: Pramanik et al. [10], with permission from Elsevier)

dependent on the particle fracture/displacement, subsequently affecting the cutting forces in machining of an MMC.

Joshi et al. [51] showed the longitudinal micrographs of typical chips formed under machining of aluminum MMCs as a function of particle volume fraction. The cutting was done on a shaper at a low-cutting speed of 16.6 m/min on an aluminum alloy with 0, 10, 20 and 30% in volume fraction of silicon carbide particles. The results indicated that as the volume fraction of the particles increased from 0 to 30% the outer profile of the chips varied from being wavy to a prominent sawtooth-like pattern which was absent at higher cutting speeds. The scanning electron microscope (SEM) images of the chip root were obtained, which clearly show that during the chip formation process fracture is initiated at the outer surface of the chips and propagates toward the tool nose while the rest of the chip is removed by plastic deformation along the shear plane.

In other experimental studies, Pramanik et al. [10] found that the chip breakability improved due to the presence of the reinforcement particles in the MMC. Short chips were formed under all conditions while with the non-reinforced alloy long and unbroken chips of almost the same length were formed under all the cutting conditions. Figure 1.6 illustrates the short and irregular shaped chips formed during machining of the MMC as a function of the feed. At lower feeds of 0.05 and 0.1 mm/rev long spiral and straight chips were observed. With a further increase of the feed (0.2 and 0.4 mm/rev), all the chips became shorter and of a C-shape. On the other hand, for the non-reinforced alloy it was found that in general the chip shape did not change with an increase in the feed or with an increase in the cutting speed (Fig. 1.7). With a variation of cutting speed, very long and brittle chips were formed for the MMC (Fig. 1.8). At lower cutting speeds (100 and

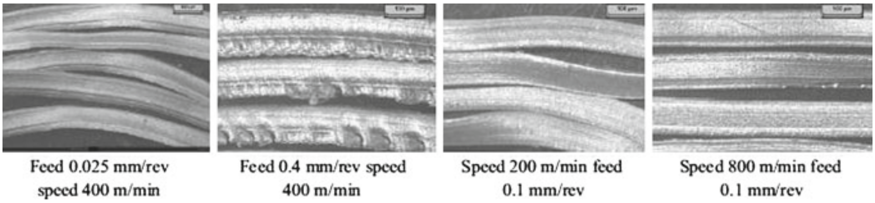
Feed 0.025 mm/rev speed 400 m/min
Feed 0.4 mm/rev speed 400 m/min
Speed 200 m/min feed 0.1 mm/rev
Speed 800 m/min feed 0.1 mm/rev

Fig. 1.7 Chip shapes of the un-reinforced alloy at different cutting conditions (depth of cut 1 mm) (*source*: Pramanik et al. [10], with permission from Elsevier)

200 m/min) all the chips were spiral in shape but at higher cutting speeds (400, 600 and 800 m/min) the chips became straight. The sawtooth nature of the chips is also clearly observable for the MMC chips as opposed to the un-reinforced alloy.

1.4.4 Cutting Forces in Fiber Reinforced MMCs

Machining studies of whisker or fiber reinforced MMC are extremely limited. Machining studies conducted on fiber reinforced polymer (FRP) composites provide a starting point in understanding the cutting mechanics of fiber reinforced MMCs. The study done by Koplev et al. [52] is considered as one of the first real attempts at understanding the machining behavior of fiber reinforced composites. They conducted orthogonal machining tests on carbon fiber reinforced polymer (CFRP) composites and observed the chip formation, surface quality and the cutting forces for two fiber orientations: perpendicular (90°) and parallel (0°) fiber orientation relative to the cutting direction. Two important results were observed: the chip formation mechanism was a series of fractures observed in the fibers and a rougher surface was observed for 90° fiber orientation samples as compared to 0° fiber orientation. In another study Takeyama and Iijma [53] described the chip formation process in machining of a glass fiber reinforced polymeric (GFRP) composite. They observed that the chip formation is highly dependent on the fiber orientation with respect to the cutting direction and observed metal-like chip formations while machining the composite with a thermoplastic matrix as opposed to a thermosetting resin polymer matrix. Kim et al. [54] conducted orthogonal tool wear tests on CFRP specimens. Fiber orientation angle and cutting speed were the major contributors to the flank wear, which was the major wear phenomenon observed. The tool wear was caused due to the very abrasive nature of the carbon fiber. It was also shown that the fiber orientation and the feed affected the surface roughness more than the cutting speed. Nayak and Bhatnagar [55] showed that the cutting force and the sub-surface damage increased with increasing fiber orientation while the rake angle had no or minimal effect on the cutting forces and the observed damage. The parameters that are the major contributors to the cutting forces, surface quality and tool wear are fiber orientation, tool geometry and

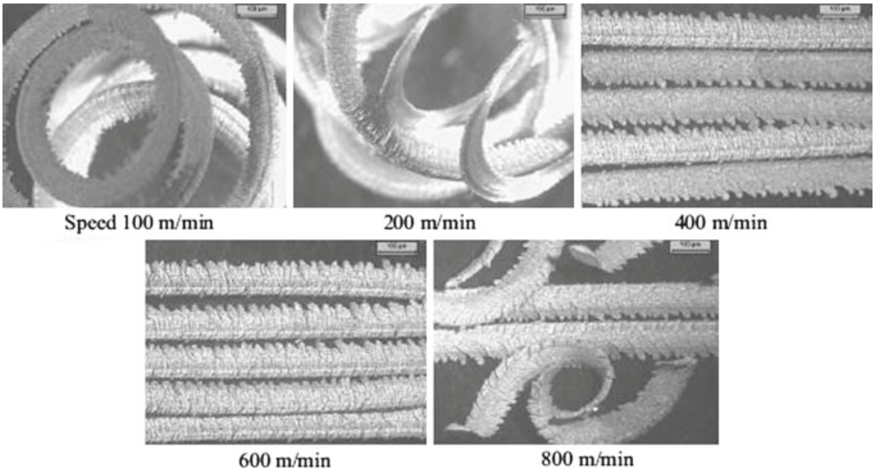

Fig. 1.8 Chip shapes of the MMC at different speeds (at feed 0.1 mm/rev and depth of cut 1 mm) (*source*: Pramanik et al. [10], with permission from Elsevier)

machining parameters. Therefore it is clear that the fiber orientation angle affects the cutting mechanics of machining fiber reinforced composites. It is postulated that the fiber reinforced MMC behaves in a manner similar to FRPs, wherein the fiber orientation plays an important role in determining the cutting mechanism.

Experimentally, Wang and Zhang [56] and Zhang et al. [57] have identified that the fiber orientation relative to the cutting direction θ is the critical parameter in determining the cutting forces and the surface integrity of the machined part. Figure 1.9 schematically shows the cutting of a long-fiber reinforced composite. The model developed here works for fiber orientations between 0 and 90°. In machining of polymer composites there are three regions of interest which are required for prediction of the cutting forces and these are shown in Fig. 1.9. In the first region, fracture occurs at the cross-section of the fibers and along the fiber-matrix interface. This region is in front of the tool rake face with the shear plane in the form of a zig-zag pattern, a result of the fibers being perpendicular to the cutting direction. In the second region, deformation takes place along the nose radius of the cutting tool where the material is pushed down (plowing). In the third region the material which is pushed down bounces back after cutting and contributes to the deformation of a long-fiber reinforced composite. Chips formed in machining of long-fiber or whisker MMCs are invariably discontinuous short chips similar to machining of thermoset polymer composites [58]. In cases where the fiber orientation angle is greater than 90°, the analysis is complicated and can only be accurately resolved numerically.

The total cutting force is a combination of the resultant deformations in the three regions identified in Fig. 1.9. In Fig. 1.9, the first region has a depth a_c and the second region equals the edge radius of the tool (r_e). The positive directions of the cutting forces are taken in the positive y and z directions as shown in Fig. 1.9.

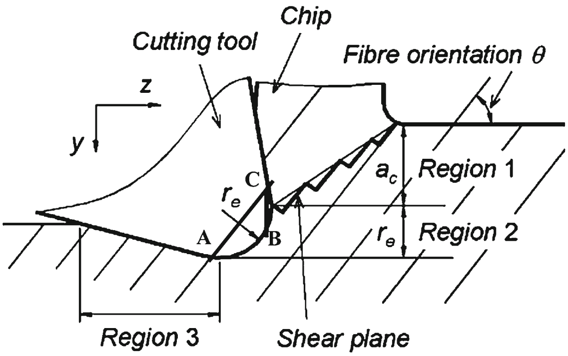

Fig. 1.9 Deformation zones when cutting long-fiber reinforced composites (*source*: Zhang [41], with permission from Elsevier)

Therefore, the total cutting force in the vertical and horizontal directions is given by F_y and F_z by Eqs. 1.18 and 1.19, respectively.

$$F_y = F_{y1} + F_{y2} + F_{y3} \tag{1.18}$$

$$F_z = F_{z1} + F_{z2} + F_{z3} \tag{1.19}$$

where F_{yi} and F_{zi} $(i = 1, 2, 3)$ are the corresponding forces in the three regions and are given by Eqs. 1.20–1.25.

$$F_{z1} = \tau_1 h a_c \frac{\sin\phi \tan(\phi + \beta + \gamma_o) + \cos\phi}{\left({}^{\tau_1}/_{\tau_2}\right)\cos(\theta - \phi)\sin\theta - \sin(\theta - \phi)\cos\theta} \tag{1.20}$$

$$F_{y1} = \tau_1 h a_c \frac{\cos\phi \tan(\phi + \beta + \gamma_o) - \sin\phi}{\left({}^{\tau_1}/_{\tau_2}\right)\cos(\theta - \phi)\sin\theta - \sin(\theta - \phi)\cos\theta} \tag{1.21}$$

$$F_{z2} = P(\sin\theta + \mu\cos\theta) \tag{1.22}$$

$$F_{y2} = P(\cos\theta + \mu\sin\theta) \tag{1.23}$$

$$F_{z3} = \frac{1}{2} r_e E_3 h \cos^2\gamma_o \tag{1.24}$$

$$F_{y3} = \frac{1}{2} r_e E_3 h (1 - \mu\cos\gamma_o \sin\gamma_o) \tag{1.25}$$

where $\phi \approx \arctan\left[\frac{\cos\gamma_o}{1-\sin\gamma_o}\right]$, E_3 is the effective modulus of the composite, h is the thickness of the workpiece, v is the Poisson's ratio, P is the resultant force and empirically given by $\frac{1}{2}\arctan\left(\frac{30}{\theta}\right)$ for the polymer composite, μ is the coefficient of friction, τ_1 and τ_2 are the shear strengths of the material in the AC and BC directions which are marked on Fig. 1.9, γ_o is the tool rake angle and β is the friction angle.

Fig. 1.10 Comparison of the model predictions vs. experimental measurements for the cutting forces for two materials. **a** Variation with depth of cut and fiber orientation for material with $E_3 = 5.5$ GPa. **b** Variation with the tool rake angle and fiber orientation for material with $E_3 = 3.5$ GPa (*source*: Zhang [41], with permission from Elsevier)

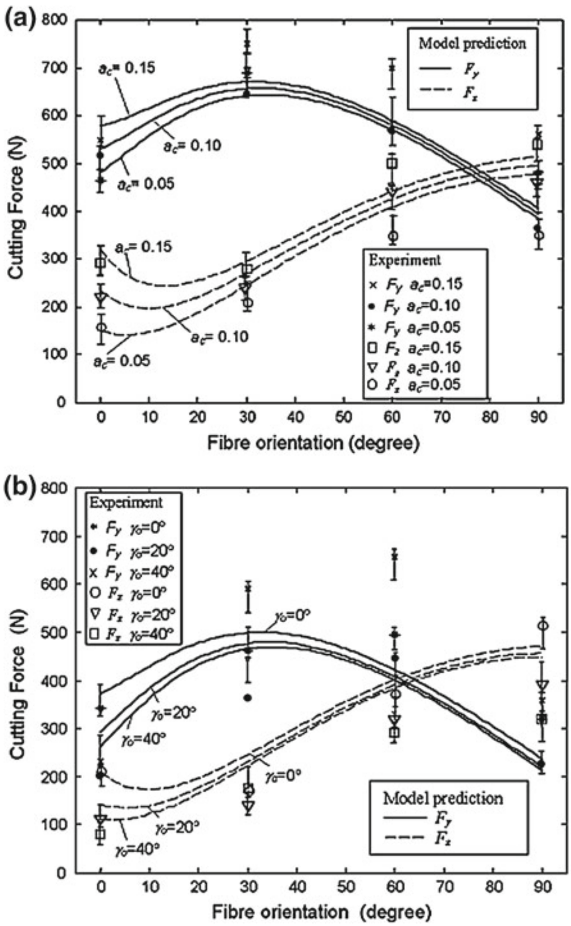

Validation of the theoretical model was done by comparing the predictions with experimental results for two long-fiber polymer composites by Wang and Zhang [56]. The authors experimentally determined the model parameters $\tau_1 = 90$ MPa, $\tau_2 = 20$ MPa, $\beta = 30°$, $\mu = 0.15$, and $v = 0.026$. Figure 1.10 shows the comparison between the model predictions and the experimental measurements for fiber angles in the range of 0–90° where the trend in the cutting force variation is well represented with the model being able to capture most of the deformation mechanisms.

Due to the limited experimental data available for machining of long-fiber MMCs, predictions for machining a MMC with $\theta = 90°$ are shown here. The workpiece material, cutting conditions and the model parameters are summarized in Table 1.3. The model predicts the cutting force (F_c) to be 53 N, while experimentally the cutting force was measured to be 49 ± 3 N. Similarly, the thrust force (F_t) is predicted to be 51.4 N which compares reasonably well with the experimental measurement of 57 ± 4 N. Experimentally, the thrust force was

Table 1.3 Cutting conditions for machining a long-fiber MMC (Dandekar and Shin [36])

Workpiece	Al-2%Cu matrix—60% by volume fraction of alumina fibers		
Tool material	PCD	E_3 (GPa)	160
Nose radius (mm)	0.8	μ	1.14
Rake angle (deg)	5	ν	0.27
Cutting speed (m/min)	30	$\tau_1 = \tau_2$ (MPa)	176
Feed (mm/rev)	0.02	$\phi(°)$	47.5
Depth of cut (mm)	0.5	r_e (μm)	20
P(N)	28.5	β (°)	48.7

consistently higher than the cutting force which is not predicted by the model. It is understandable that the model will not be able to capture the entire deformation phenomena during machining of MMCs, especially since the model was developed for FRP machining. Nonetheless it provides a reasonable estimate of cutting forces and also reiterates the importance of numerical modeling.

1.5 Finite-Element Modeling in Machining

A tremendous amount of research has been done in understanding the mechanics associated with machining processes. Compared to empirical or analytical methods, the development of computers has allowed researchers to study machining through sophisticated numerical techniques. These include finite-element modeling, molecular dynamics studies and recently multi-scale modeling. In this chapter only the former modeling technique is addressed. Despite the success in modeling 2D and 3D machining, there are still many challenges associated with modeling of machining. A bibliography of all the finite-element modeling research done from 1976 to 2003 for machining was compiled by Mackerle [59, 60]. Over 300 papers have been referenced in this bibliography. In spite of this, research in this field continues to grow. Active research continues to provide an understanding of the constitutive behavior of materials, chip formation, modeling of composite machining, tool–chip interface behavior, etc. The approaches that have been used for numerical modeling of machining processes range from atomistic level techniques to macro level continuum mechanics methods. Despite these efforts problems have not yet been completely solved due to the extreme complexity involved in machining processes.

1.5.1 FEM Formulations and Approaches

In FEM, three main formulations have been proposed for machining simulations: Eulerian, Lagrangian and Arbitrary Lagrangian Eulerian (ALE) methods. In the Eulerian method, mesh is spatially fixed while material is allowed to flow through the meshed control volume. The advantage of the Eulerian method is that the excessive element distortion is absent since the mesh is fixed. The disadvantage is that the initial shape of the chip and the contact conditions are needed to be known in advance and hence it is not suitable for machining simulations. In the Lagrangian approach on the other hand the mesh is attached to the workpiece and the elements are allowed to deform similarly to machining. This method has been the most popular method in machining simulation as the chip geometry does not have to predefined, but rather develops as the cutting progresses. However it is dependent on a defined chip-separation criterion [61]. The disadvantage of the method is the excessive element distortion and the need for frequent remeshing that is computationally expensive. The ALE is an adaptive meshing technique that combines pure Lagrangian and Eulerian formulations to incorporate the advantages of both. In the ALE method, the finite element mesh is neither fixed spatially nor attached to the material. Instead it is allowed to flow with the material [62]. In this manner severe distortion of the elements is avoided without the need for remeshing. The ALE method has successfully been implemented in machining simulation to predict chip formation in metal cutting by numerous authors [63–70]. A good review on FEM of metal cutting was provided by Soo and Aspinwall [61] for the interested reader.

Numerous numerical modeling studies have been conducted on orthogonal machining of composite materials. Three primary approaches have been successfully implemented: (a) a micromechanics-based approach (b) an equivalent homogeneous material (EHM) based approach and (c) a combination of the two approaches. The micromechanics and the equivalent homogenous material (EHM) based approaches have their respective advantages and disadvantages [71]. The micromechanics approach describes the material behavior locally, and hence it is possible to study local defects such as debonding and complicated deformation mechanisms especially in fiber reinforced composites. The required computation time however, is very high since to predict local damage the mesh used for this study is a lot finer than the one needed for the EHM model. On the other hand the EHM approach reduces the computation time but is not capable of predicting the local effects, namely, the damage observed at the fiber-matrix interface [72–74]. Therefore there is a need to harness the advantages of both the continuum and micromechanics models in their capabilities of predicting cutting forces and sub-surface damage. Rao et al. [75, 76] used a combination of the EHM and micromechanical model to model 2D orthogonal cutting and study the effect of fiber orientation on the simulated cutting forces, chip formation, the extent of fiber damage, matrix damage and debonding. The micromechanical model was used in the vicinity of the tool, while the EHM model was implemented away from the tool.

1.5.2 Constitutive Materials Modeling

In any FEM model an essential input is the accurate definition of material properties. Under machining conditions, generally the workpiece is subjected to extreme deformation involving high levels of strain and strain rates and rapid temperature rise. The workpiece material is usually modeled by constitutive equations describing the stress-strain response together with its dependence on strain rate, temperature and work hardening. Furthermore in the Lagrangian or ALE analysis there is a necessity to include a chip-separation criterion. This chip-separation criterion triggers the material fracture resulting in separation of a chip from the workpiece. To achieve this one must be able to accurately describe the fracture behavior to represent the material under study through an appropriate damage model. Any constitutive model selected for the material needs to be validated prior to inputting into a finite-element model.

In machining simulations when using an EHM approach for the machining of the composite, homogenization of the material is necessary. Traditional homogenization techniques based on either exact or energy methods are useful primarily in the elastic regime of the composite. In machining a high degree of plasticity is involved in the primary and secondary shear zones, and extremely high-strain rates and temperatures are also observed. Therefore one also needs a description of the plastic deformation of the composite material and also its behavior at high temperatures and high strain-rates. To this end a number of empirical constitutive models have been presented for modeling the deformation behavior at high strain-rates and temperatures: for instance, the widely used Johnson–Cook (J–C) equation [77] and the Norton-Hoff law [78, 79]. The Norton-Hoff material model was applied by Monaghan and Brazil [22] to model the machining of a particulate reinforced MMC while the J–C model has been successfully applied to the modeling of a silicon carbide particle reinforced aluminum matrix composite [80, 81]. The Johnson–Cook equation is based on experimentally determined flow stress as a function of strain, temperature and strain rate in separate multiplicative terms. This equation therefore does not consider the interactions between the terms. The model is relatively easy to apply in the FEM setting and hence has been used in many studies. The important aspect in applying this model is the relevance of the experimental data as it needs to cover material deformation under a range of strains, strain rates and temperatures typically seen in machining and hence it is expected to obtain data from a number of resources. One caveat in using empirical models is that its choice significantly influences the predicted results [61] and so it is extremely critical to choose the right material model and parameters.

On the other hand for carrying out multi-phase modeling, good material models for the reinforcement and matrix along with the interface are necessary inputs. Once again dependent on the reinforcement or the matrix it is necessary to select an appropriate material model. A number constitutive models are available in the literature to model the matrix material; Zerrili–Armstrong (Z–A) type constitutive model [82], a Johnson–Cook type model [77], Mecking–Kocks model [83] and a physics-based model proposed by Nemat-Nasser et al. [84] for OFHC copper etc. Another material model successfully applied to modeling machining of an aluminum MMC is the Cowper–Symonds (C–S) model for the 6061 aluminum matrix [19]. Any model that is able to capture the high adiabatic shearing observed during machining of MMCs is suitable for simulations. Since both categories, phenomenological and physics-based model, determine material constants by fitting to stress-strain responses at different temperatures and strain rates, the advantage in using one model over another is merely dependent on the number of constants to determine. The Meckings–Kocks model has 23 constants, 12–8 constants are necessary to use the Nemat-Nasser and Li model depending on the inclusion of dynamic strain aging or not, Z-A model needs seven constants but modification to the Z–A model can reduce the number of constants to six [82], the J–C model needs only 5 constants while the C–S model has two fitting parameters. Most of these models have the ability to model the material response as close to experimental data and hence there is always an advantage in using a material model with fewer constants. An advantage of using the Z–A or J–C model is that a number of studies have been conducted to calculate the material constants for aluminum, steel, titanium etc., which are widely available.

The brittle reinforcement materials are usually modeled as linearly elastic materials with damage initiation being instantaneous and hence do not need a damage evolution law in machining simulations. Material properties for a popular reinforcement material of alumina and silicon carbide particles are provided in Tables 1.4 and 1.5. Once again the material properties can be obtained from experimental readings or in some cases through atomistic simulations carried out with techniques such as molecular dynamics. Material failure in the reinforcement is related to the critical stress to the damage equivalent stress at failure. The material is considered failed once the critical stress equals the ultimate tensile stress of the material [85]. Another method for brittle materials was applied by Marusich and Ortiz [86], who applied a failure criterion based on the effective plastic strain of ductile failure. The failure occurred when the stress attained a critical value as determined by the fracture toughness of the material.

The interface between the reinforcement phase and matrix phase plays a crucial role in the analysis of damage or failure in a composite material. Modeling of the interface in a composite structure is achieved through the use of interface elements. A number of different approaches have been considered for interface elements [90] but in general the interface elements function in a similar manner, wherein they connect the two phases while transferring the traction between them until a predefined displacement criterion is reached, at which point the interface element degrades in material stiffness, hence carrying no load. The functional relationship is defined by a traction-displacement relationship. Cohesive elements, a type of interface elements, are widely used to model delaminations and debonding in composite structures as it considers both damage and fracture mechanics and have been successfully applied to composite machining simulations [36, 55, 74, 91]. The interested reader in understanding the application and numerical implementation of the cohesive zone model is encouraged to review the work done by Needleman [92], Tvergaard [93], Xu and Needleman [94], Camacho and Ortiz [95] and Chandra et al. [96] who have studied the application of the cohesive zone model to simulate the metal-ceramic interfaces.

Table 1.4 Mechanical properties of alumina fiber (Nextel$^{\text{TM}}$ 610) [87, 88]

Diameter (μm)	14–20
Modulus of elasticity (GPa)	373
Tensile strength in fiber direction (S11) (MPa)	3,100
Compressive strength in fiber direction (S11) (MPa)	3,360
Tensile strength in transverse direction (S22) (MPa)	318
Compressive strength in transverse direction (S22) (MPa)	362
Density (ρ) (kg/m^3)	3,900
Poisson's ratio	0.27
Melting temperature (°C)	2,000
Coefficient of thermal expansion/°C (range: 100–1,100°C)	8×10^{-6}

Table 1.5 Properties of silicon carbide [89]

K	Fracture toughness	3.9 MPa
E	Youngs modulus	408 GPa
v	Poisson's ratio	0.183
ρ	Density	3.2 gm/cm^3
α	Coefficient of linear thermal expansion	5.12×10^{-6}/°C

1.5.3 Chip-Separation Criteria

Material separation is a complex phenomenon involving many physical processes occurring at the micromechanical level. Fracture begins at the micromechanical scale and eventually with damage accumulation macroscopic fracture is observed. In FEM simulations, the variables that control fracture are the current variables of stress and strain tensors and their histories. Damage initiation is dependent on the current stress/strain state while damage evolution is dependent on the history of the stress/strain state. Some of the damage criteria used today, either built-in in commercial FEA codes or through the implementation of user-defined subroutines for machining simulations, are: (a) constant equivalent strain criterion, (b) maximum shear stress criterion, (c) Johnson–Cook fracture model and (d) Cockroft–Latham criterion. The equivalent strain criterion has been a popular failure criterion for metal cutting simulations [19, 97–99]. In this approach fracture is assumed to occur at the material nodal points when the equivalent plastic strain reaches a critical value dependent on the material. On reaching the critical value the node in front of the tool tip is separated from the workpiece, resulting in chip formation. The drawback of this method is the node separation technique that is computationally intensive and tedious. Similarly a critical stress criterion has also been suggested where node separation is activated once the material reaches a critical stress value [100]. The Johnson–Cook failure criterion is based on the postulation that the critical equivalent fracture strain is a function of the stress triaxiality, strain rate and temperature. The fracture model is semi-empirical in nature and necessitates the determination of constants from tensile tests with high triaxility, shear tests and Hopkinson bar torsion tests at varying temperatures and strain rates, and has been used to model machining of a particulate MMC [80]. This limits the use of the model as a number of experiments are needed to arrive at the five material constants necessary in implementing the model. Another fracture model implemented in machining codes is the Cockcroft–Latham fracture criterion [101, 102]. This criterion is widely used in machining simulations, such as predicting serrated chip formations as is the case with titanium machining. The criterion was developed for bulk forming operations and therefore there is a limitation on its application, as it is applicable only in small and negative triaxiality situations. Fracture in this model occurs when the equivalent strain modified by the principal tensile stress reaches a predefined critical value.

1.5.4 Friction at the Tool–Chip Interface

Another parameter important to the accuracy of numerical machining simulations is the influence of the friction conditions at the tool–chip interface. Friction at the tool–chip interface is a very complex process. One of the methods is to experimentally obtain the coefficient of friction and apply it as a constant over the tool–chip contact length. In most studies, the Coulomb friction model is commonly used as in machining simulations. In their machining simulations of a 20% by volume fraction of particulate (SiC) in an aluminum matrix, Pramanik et al. [19] used a Coulomb friction law and Tresca shear stress limit to model the sticking and sliding conditions at the tool–chip interface. In their study, the friction at the tool–chip interface is controlled by a Coulomb limited Tresca law which is expressed by Eqs. 1.26 and 1.27.

$$\tau = \mu \sigma_n \tag{1.26}$$

$$|\tau| \leq \tau_{\lim} \tag{1.27}$$

where $\tau_{\lim}$ is the limiting shear stress, τ is the equivalent shear stress, μ is the friction coefficient and σ_n the normal stress (contact pressure). According to this model the two contacting surfaces carry shear stresses up to a certain magnitude prior to starting sliding relative to each other. When $\tau > \tau_{\lim}$ the two surfaces slide relative to each other. The limiting shear stress was 202 MPa and the coefficient of friction was modeled as 0.62 [19].

Recently, Filice et al. [103] analyzed the influence of different friction models on the results of numerical machining simulations. They concluded that for the studied workpiece/tool couple, most mechanical results are not influenced by the friction model except the temperature at the tool–chip interface. Nonetheless the accurate representation of the coefficient of friction allows for accurate prediction of cutting forces and temperature distributions.

1.6 Modeling of MMC Machining

It is clear that the presence of reinforcement makes MMCs different from monolithic materials due to incorporation of its superior physical properties. Different failure mechanisms play an important role during the machining of MMCs: (1) cracking of the reinforcing particles; (2) partial debonding at the particle/matrix interface resulting in the nucleation of voids and (3) the growth and coalescence of voids in the matrix. From the previous section on analytical modeling of MMCs machining it is understood that these models are not able to adequately handle all the aforementioned failure phenomena which contribute to the machining performance of the MMC. To handle the tool–reinforcement interaction, finite element simulations of machining have been used. Finite element simulations have been able to successfully predict phenomena such as: (1) flow of particles in the chip root region, (2) debonding of the particles in the secondary cutting zone and sub-surface, (3) tool–workpiece (particle) interaction, (4) pull-out of the particles and (5) fiber debonding and fiber damage in a fiber reinforced MMC.

1.6.1 Modeling Machining of Particulate reinforced MMC

A number of attempts have been made in modeling machining of MMCs [19, 23, 36, 48, 80, 104]. Except for the study done by Dandekar and Shin [80] all the other studies have primarily focused on 2D modeling of orthogonal cutting, which is not realistic for actual machining. Monaghnan and Brazil [48] studied the failure at the particle-matrix interface and the residual stress in machining MMCs using the 2D finite element code FORGE2 for an A356 aluminum alloy reinforced with 30% by volume fraction of silicon carbide, but tool–particle interaction was neglected. El-Gallab and Sklad [23] simulated the residual stresses and sub-surface damage observed in a SiC particle reinforced aluminum alloy and concluded that the feed had the largest effect on the sub-surface damage and the simulated residual stresses, wherein damage and residual stress increased with an increase in the feed. This study, focused on predicting sub-surface damage, lacked in their representation of the interface, since the particles are considered to be perfectly bonded to the matrix, and was concerned with 2D orthogonal machining. Later, others studied the tool–particle interaction by considering particles along, above and below the cutting path [19, 104] as shown in Fig. 1.11.

This section further provides an example for setting up an FEM for modeling machining of particulate MMCs. For the orthogonal machining simulation of particulate reinforced MMC a combination of 2D plane strain continuum quadrilateral (CPE4R) and triangular (CPE3) elements are used for meshing the particles and matrix, while the interface layer is modeled using the 2D cohesive elements. A plain strain analysis is generally used in modeling orthogonal

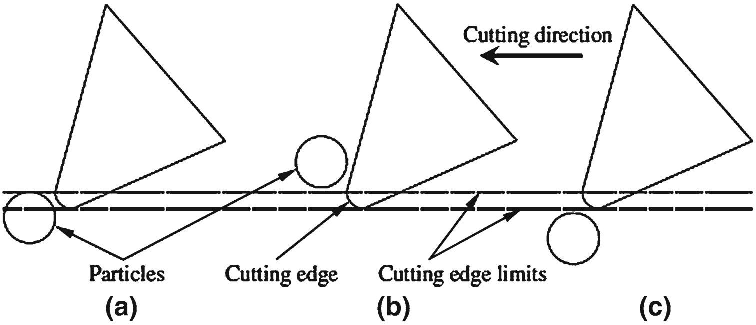

Fig. 1.11 Particle locations with respect to the cutting path: particles **a** along, **b** above and **c** below the cutting path (*source*: Pramanik et al. [19], with permission from Elsevier)

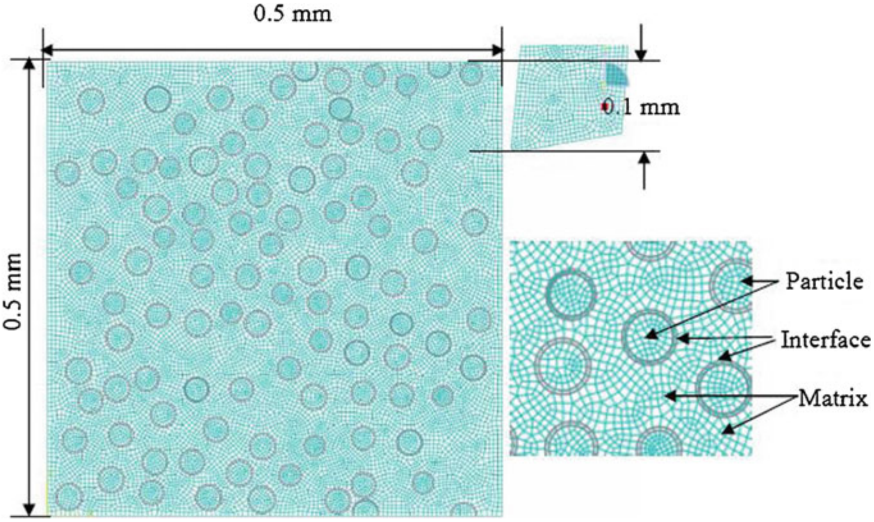

Fig. 1.12 **a** FEM mesh for modeling of machining a particulate MMC showing the length scales. **b** Close-up of the mesh

machining for homogenous materials. The MMC due to the random distribution of particles behaves in a homogenous manner. The random distribution of the particles is carried out using a random particle distribution scheme which is explained later. A representative mesh for the particulate reinforced MMC is shown in Fig. 1.12. For the simulation the boundary conditions applied are as follows; the workpiece is constrained to move in both the (x) and (y) directions at the bottom side, left-hand side and the lower right-hand side. The tool is given a constant velocity in the (x) direction and the tool movement in the (y) direction is constrained. The tool material simulated is a PCD tool with a nose radius of 0.4 mm

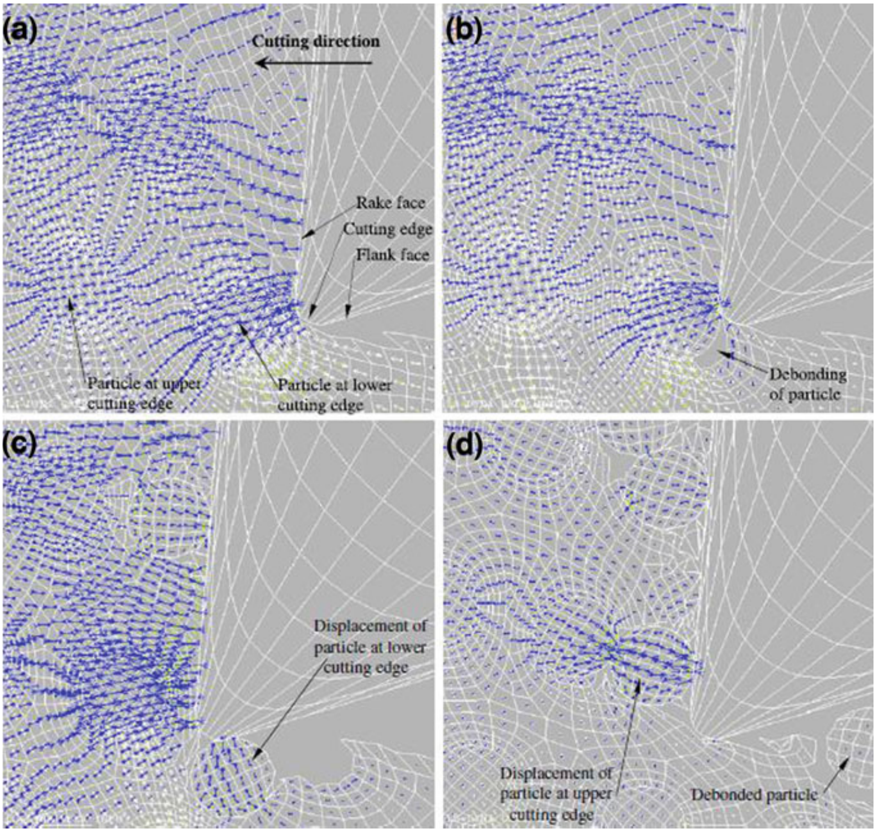

Fig. 1.13 Evolution of stress fields for particles along the cutting path. Compressive and tensile stresses are represented by *black* >-< and *white* <-> symbols, respectively. Their lengths represent the comparative magnitudes (*source*: Pramanik et al. [19], with permission from Elsevier)

and a rake angle of 5°. The cutting conditions are as follows; feed rate of 0.1 mm/rev, depth of cut of 0.25 mm and a cutting speed of 200 m/min.

1.6.1.1 Tool–Particle Interaction

Pramanik et al. [19] conducted an extensive study to characterize the evolution of the stress field and the development of the plastic zone in orthogonal machining of a 20% by volume fraction SiC in a 6061 aluminum matrix. The authors divided the scenarios into three categories: (1) particles along the cutting path, (2) particles above the cutting path and (3) particles below the cutting path.

In the first scenario, the particle is along the cutting path and interacts between the upper and lower limits of the cutting edge as shown in Fig. 1.13a. The evolution of the stress fields during machining in this scenario is captured in

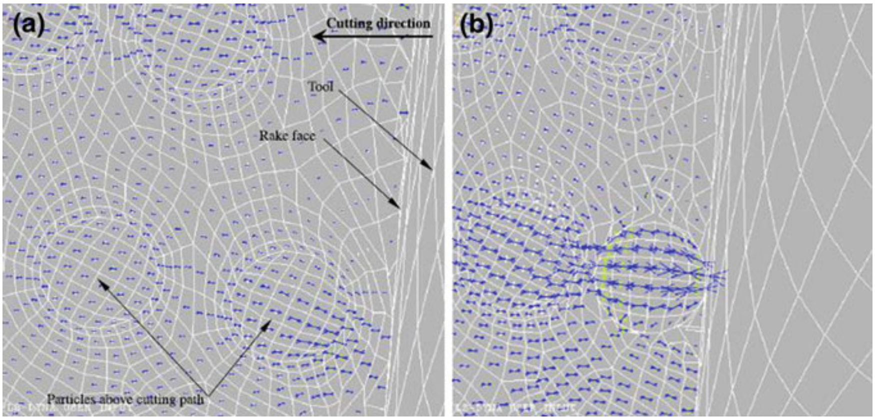

Fig. 1.14 Evolution of stress fields for particles above the cutting path. Compressive and tensile stresses are represented by *black* >-< and *white* <-> symbols respectively. Their lengths represent the comparative magnitudes (*source*: Pramanik et al. [19], with permission from Elsevier)

Fig. 1.13a–d. For a particle located in the lower part of the cutting edge, compressive and tensile stresses are perpendicular and parallel in front of the cutting edge causing possibly fracture of the particles and debonding at the interface. In the simulations particle fracture was not observed as the material definition of the SiC particles lacked any failure criteria. Upon advancement of the tool, the matrix along the upper part of the particle and tool becomes highly compressive while the lower-right interface of the particle becomes tensile (Fig. 1.13a), resulting in the debonding of the particle with the advancement of the tool. During tool–particle interaction significant tensile and compressive stresses are found to be in the left part of the particle (Fig. 1.13b) with the right corner experiencing compressive stress. Upon further advancement of the cutting tool, the particle debonds and plows through the matrix creating a void (Fig. 1.13c) and then slides along the flank face of the tool (Fig. 1.13d). The particle located at the upper part of the cutting edge moves slightly upward due to the plastic flow of the matrix. The stress distribution in this state also promotes particle debonding and/or fracture. Upon further advancement of the cutting tool the two particles interact with each other and are consequently under highly compressive stresses which may cause fracture of the particle as well as contribute to the wear of the flank face.

In the second scenario for particles above the cutting path, the evolution of the stress fields is shown in Fig. 1.14a and b. At the start of machining highly compressive stresses perpendicular to the tool rake face through the particle and in the matrix between the particle and the rake face are observed. Additionally, parts of the particle and the interface are under compressive and tensile stresses as shown in Fig. 1.14a. The combination of this stress state may initiate particle fracture and debonding. Upon further advancement of the cutting tool, the particle partially debonds and the contact region where the particle interacts with the rake face is

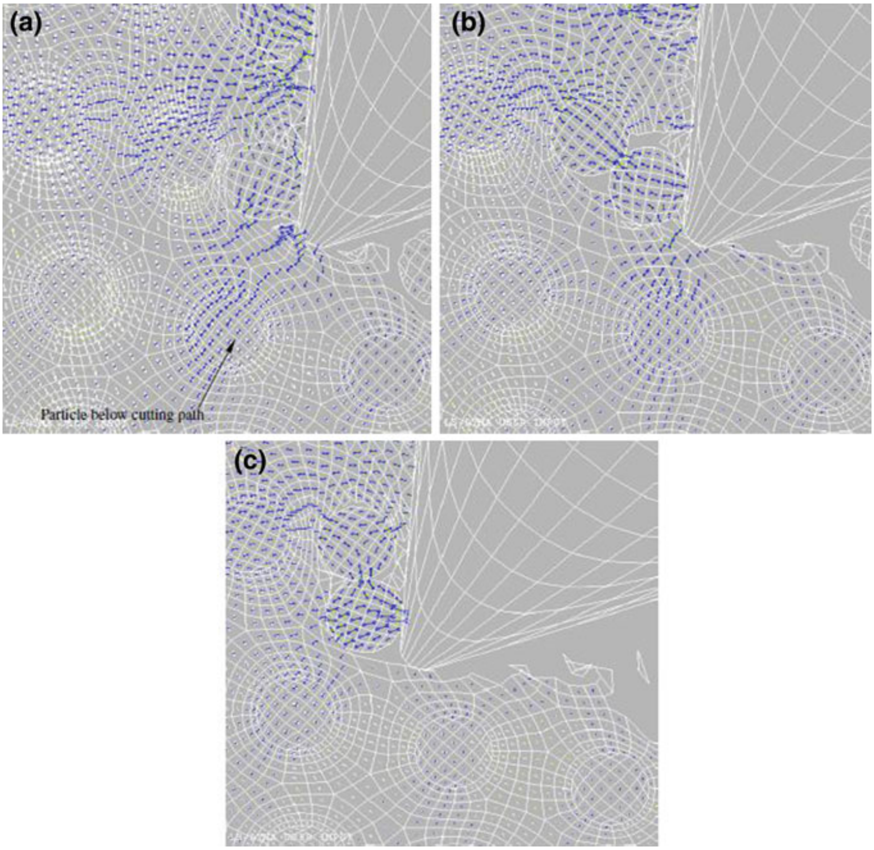

Fig. 1.15 Evolution of stress fields for particles below the cutting path. Compressive and tensile stresses are represented by *black* >-< and *white* <-> symbols respectively. Their lengths represent the comparative magnitudes (*source*: Pramanik et al. [19], with permission from Elsevier)

under high-compressive stresses and encourages particle fracture. Further advancement of the tool, the first particle then interacts with the second particle and slides across the rake face of the tool (Fig. 1.14b).

In the third scenario of the particle below the cutting edge, the stress distribution in the particle and matrix has a direct influence on the residual stress of the machined part. As the tool approaches the particle, the matrix between the cutting edge and particle is under compressive stresses acting in a radial direction to the cutting edge (Fig. 1.15a–c). In this configuration the particle and the matrix are under compressive and tensile stresses which act in the radial direction. Once again this stress distribution promotes particle debonding and void formation in the matrix. When the tool passes over the particle the direction of the tensile stresses becomes parallel to the machined surface while the compressive stresses remain radial to the cutting edge. The newly generated surface (Fig. 1.15c) is

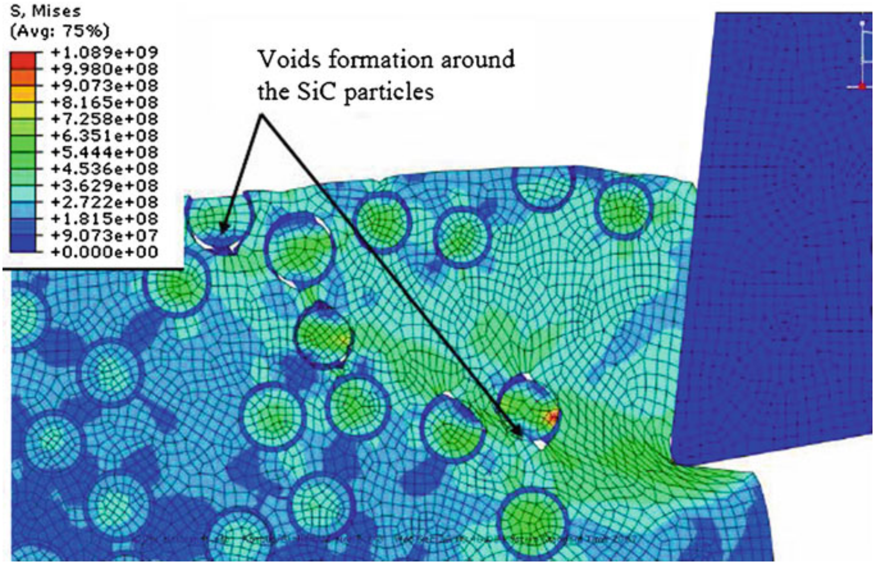

Fig. 1.16 Machining simulation of Al/SiCp MMC showing the failure of the interface

under compressive residual stresses which are parallel to the machined surface. Similar observations were reported by Quan and Ye [105] in their study on machining of a SiC particulate reinforced MMC.

1.6.1.2 Chip Formation and Debonding

The physical deformation phenomenon during machining of MMC is captured well in the model described in Dandekar and Shin [80]. There is distinct shear localization at the initial debonding sites along the interface appearing as a shear band (Fig. 1.16). The particle distribution has a strong effect on the formation and intensities of shear bands between the particles, as well as on the concentration of stress maxima in the vicinity of the particles. This high-stress/strain region along the interface results from the high difference in the elastic modulus between the matrix and the reinforcing particle.

The simulation results are compared to the experimental observations by El-Gallab et al. [8]. The authors concluded that the failure in the composite initiates along the voids which are formed around the SiC particles. The chip formation was segmented and discontinuous with ductile tearing at the edges due to the alignment of the SiC particles. The voids join up forming micro-cracks and subsequent fracture along the shear band. All these observations are clearly seen in the simulations, where there is first void formation along the particles, then alignment of the particles and finally fracture along the shear band (Figs. 1.16, 1.17, 1.18, 1.19).

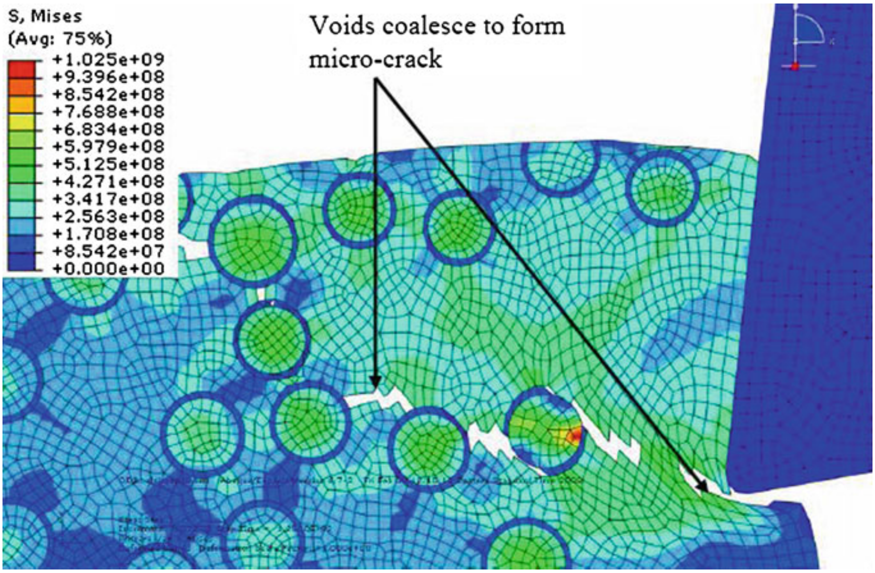

Fig. 1.17 Machining simulation of Al/SiCp MMC showing the void coalescence

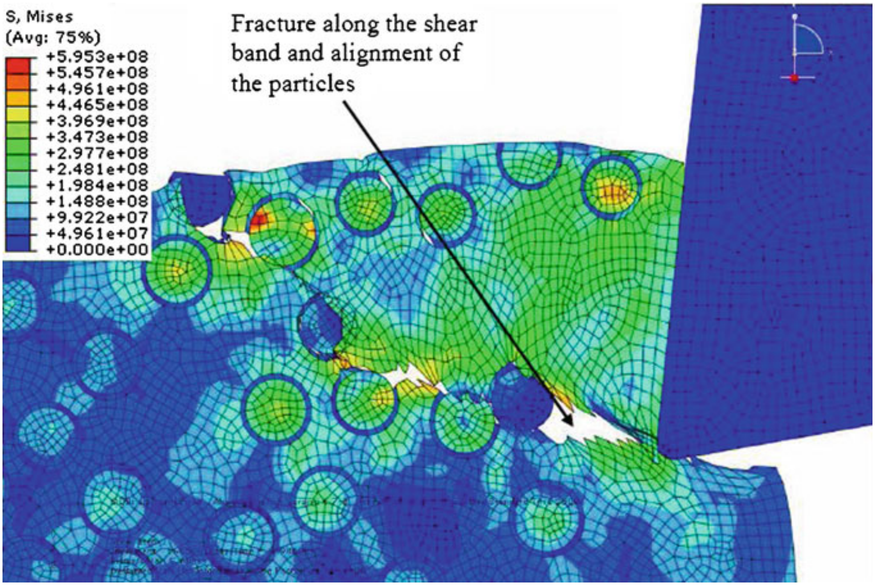

Fig. 1.18 Machining simulation of Al/SiCp MMC showing fracture and alignment of particles

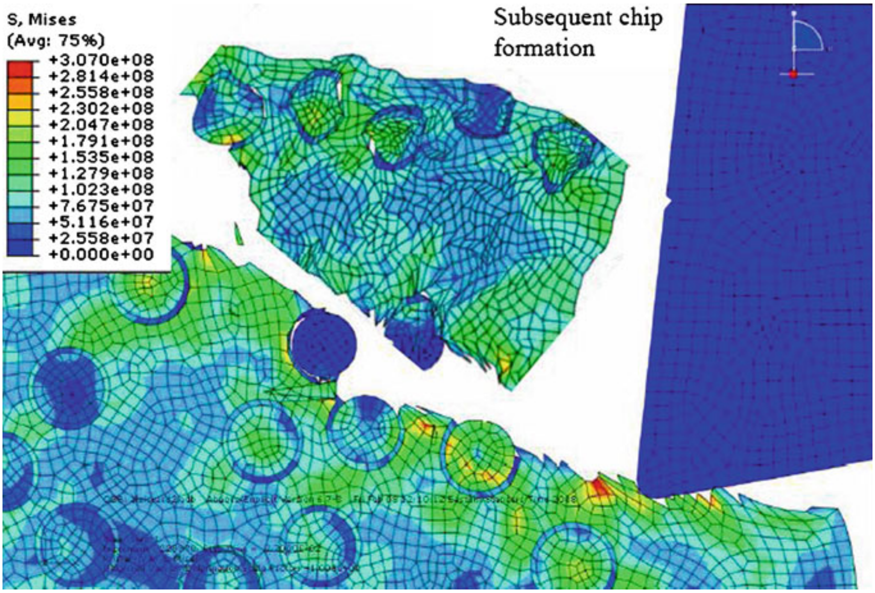

Fig. 1.19 Machining simulation of Al/SiCp MMC subsequent chip formation

1.6.1.3 Numerical Predictions of Cutting Temperature

It was previously shown that theoretical calculations are inadequate in predicting the cutting temperatures in machining. An attractive alternative is to utilize numerical methods such as finite-element models. A number of studies have been conducted in modeling the heat transfer mechanisms involved during the cutting of a metal matrix composite [6, 43, 104, 106, 107].

Among these studies, Zhu and Kishawy [104] simulated the machining of a 10% by volume fraction of Alumina in an aluminum alloy 6061 matrix. The machining model setup corresponds to an orthogonal machining model with particles randomly distributed in the matrix. The two-dimensional orthogonal cutting process was simulated using the commercially available finite element solver ABAQUS/Explicit using the ALE formulation. Two-dimensional four-node displacement and temperature continuum elements featuring reduced integration and hourglass control are used to carry out the coupled temperature-displacement analysis.

The authors identified three main heat sources in the secondary deformation zone: the plastic deformation in the chip which is in contact with the tool rake face, the heat generated due to friction along the tool–chip interface, and the heat generated due to the chip sliding across the rake face. The results indicated that the tool–chip interface friction is the most important factor in the increasing temperature. Figure 1.20a–c shows the contour plots of the temperature for feeds of 0.1, 0.2 and 0.3 mm/rev, respectively. The temperature generated along the tool–

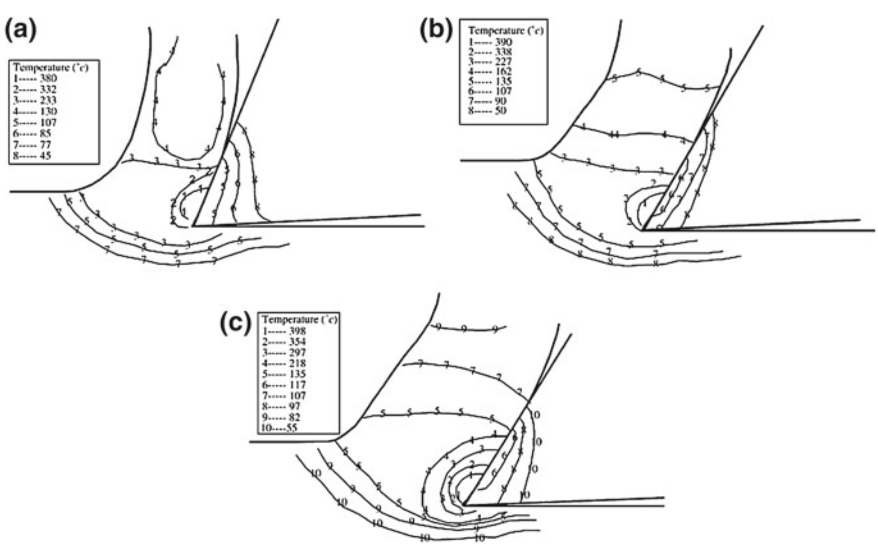

Fig. 1.20 Temperature distribution on the matrix. **a** Temperature contour for feed = 0.1 mm/rev. **b** Temperature contour for feed = 0.2 mm/rev. **c** Temperature contour for feed = 0.3 mm/rev (*source*: Zhu and Kishawy [104], with permission from Elsevier)

chip interface is substantially higher than that in the primary shear zone. At a cutting speed of 85 m/min and at feeds of 0.1, 0.2 and 0.3 mm/rev, the maximum temperatures predicted along the tool–chip interface were 380, 390 and 398°, respectively. According to the authors, the large amount of heat generated in the primary shear zone and the increase in the temperature are entirely related to the plastic deformation. An expected result is the higher temperatures with an increase in the feed.

Other studies on temperature predictions in machining of MMCs are concerned with the temperature observed on the cutting tool [43, 107]. The authors compared experimentally measured cutting temperatures to simulation predictions. The commercially available FEM solver ANSYS was used in the heat transfer analysis. Experiments were conducted on an A359 aluminum alloy reinforced with 20% by volume fraction of silicon carbide particles using a CVD-coated diamond insert. Cutting temperatures were measured using K-Type thermocouples along the locations schematically shown in Fig. 1.21.

A heat transfer model of the 3 D tool was constructed in ANSYS. In this model, transient heat conduction with adiabatic boundary conditions was applied for an initial machining temperature of 21°C. Convection boundary conditions with relative air flow caused by workpiece rotation were neglected as it showed negligible effects. At the tool–chip interface, the thermal boundary condition is uniformly specified as a heat flux, $\beta_r q_r$, where q_r is the overall heat flux at the rake face and β_r the heat partition index. The overall heat flux is due to the friction at the tool–chip interface and is determined by $(F_f/V_c)/A_c$, where F_f is the frictional

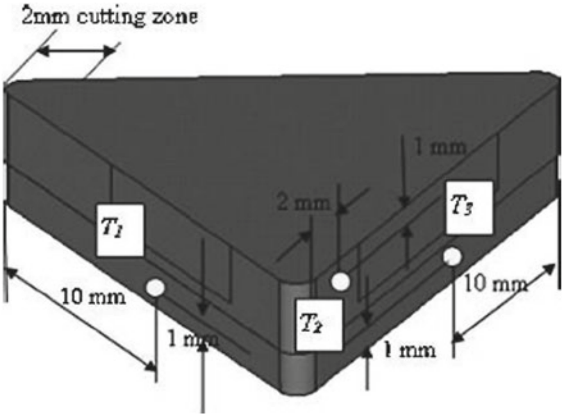

Fig. 1.21 Temperature measurement locations are marked as T_1, T_2 and T_3 of the K-Type thermocouples (*source*: Liu and Chou [43], with permission from Elsevier)

force, V_c is the chip sliding velocity and A_c is the tool–chip contact area, which are experimentally measured or determined through analytical models. The heat partition coefficient was numerically calculated by modeling a 2D chip model consisting of a long strip with chip thickness as the width dimension and the other dimension being relatively long to simulate an infinite domain. The model has a heat source, heat flux, and the tool–chip contact length, moving with the chip velocity along the boundary of the chip zone. The initial temperature of this chip model is the shear plane temperature calculated from theoretical models. In this manner the heat partition coefficient is determined numerically. Figure 1.22 shows the 3 D tool model used for predicting the tool temperatures. It was found that the cutting speed dominates the temperature rise of the cutting tool and the results qualitatively agreed with the temperature measurements from machining. The comparison of the simulated predictions with experimental measurements is given in Table 1.6.

1.6.1.4 3D Modeling of Sub-Surface Damage

The FEM machining model described in the previous section provides an insight into stress distributions when machining of an MMC. Practical machining is not a 2D process; therefore to circumvent this problem Dandekar and Shin [80] proposed a multi-step 3D FEM simulation for prediction of cutting forces and machining induced sub-surface damage in an A359/SiC/20p composite. The multi-step approach combines two modeling strategies: (a) a micromechanics-based approach and (b) an equivalent homogeneous material (EHM)-based approach. In the first step an EHM model is used for the overall prediction of cutting forces, temperature and the stress distributions in the composite undergoing machining (Fig. 1.23a). Three regions are chosen to calculate the sub-surface damage as marked on Fig. 1.23a. The actual locations of these regions are on the machined surface below the cutting tool near the marked areas. The resultant stress and

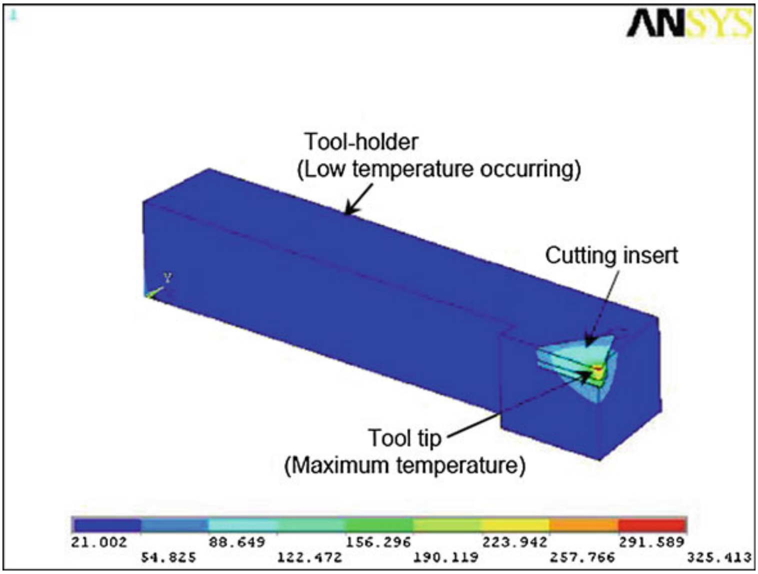

Fig. 1.22 Simulated cutting temperature distributions in the cutting tool (*source*: Chou and Liu [107], with permission from Elsevier)

Table 1.6 Comparisons between simulation and measured tool temperatures

		Simulation predictions (°C)			Experimental measurements (°C)		
Speed (m/min)	Feed (mm/rev)	T_1	T_2	T_3	T_1	T_2	T_3
60	0.1	84.1	72.5	72.9	66	65.5	71
60	0.3	99.9	87	87.2	77	90	97
180	0.1	102.4	89	89	87	91	99.5
180	0.3	97.1	81	81.3	95	81.5	87.5

Source: Liu and Chou [43], with permission from Elsevier

temperature from the 3D EHM model are subsequently imported into the local model (Fig. 1.23b. In the EHM model regions of 100 μm × 100 μm × 100 μm are selected along the cutting path at different locations in the workpiece. The post-processing is done in Third Wave Systems AdvantEdge$^{\text{TM}}$ to obtain the stress and temperature distributions. The 3D microstructure of the local model is generated using the RSA (Random Sequential Adsorption) algorithm proposed by Rintoul and Torquato [108]. In the local model, the particle and matrix are assigned individual material properties, while the interface layer is modeled using 3D cohesive zone elements. Model details, boundary conditions, mesh size, convergence studies and validation of the material properties input in the FEM simulation can be obtained from Dandekar and Shin [80] and are not repeated here. In this manner the model harnesses the advantages of both the continuum (computational

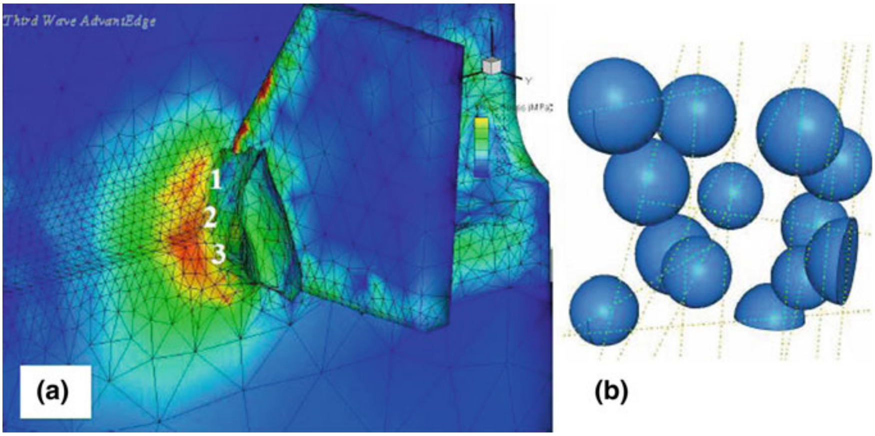

Fig. 1.23 **a** Stress distribution obtained from machining simulation software of a EHM MMC model using the 3D nose turning option in Third Wave Systems AdvantEdge code. **b** Multiparticle spheres in a random arrangement for 20% volume fraction (*source*: Dandekar and Shin [80], with permission from Elsevier)

speed and simplicity) and micromechanics (consideration of local effects) models, enabling it to accurately predict cutting forces and sub-surface damage.

The authors conducted machining tests on cast cylinders of A359/SiC/20p composites, supplied by MC-21 Inc. in the form of 68.5 mm diameter cylinders with a cut length of 152.4 mm. Each cutting test was repeated and the final plotted value of the cutting force Fig. 1.16 is an average of the steady state values for the two experiments conducted under the same cutting condition. For the measurement of damage, a scanning electron microscope was used to take five measurements from each of two different samples for all the cutting conditions. The reported value is the average value of these 10 measurements. A variation of 10–15% was observed in the experimental measurements.

At a cutting speed of 150 m/min and a feed rate of 0.05 mm/rev the simulated values of the cutting and thrust force were 78 and 56 N, respectively. On the other hand at a feed rate of 0.1 mm/rev the simulated cutting and thrust forces were found to be 126 and 55 N, respectively. The simulated cutting force and thrust force for the condition of 300 m/min cutting speed and a feed rate of 0.05 mm/rev were 80 and 56 N respectively. For the case of feed rate of 0.1 mm/rev the simulated results were 128 and 55 N, respectively. The coefficient of friction used in the simulations for all the cases was calculated from the experimental data.

On the whole the cutting forces as well as the thrust force match very well with experimental data. The trend observed in all the cases is similar such that the simulation under-predicts the cutting force by 7–8% and the thrust force by 6–12%. Figure 1.24 shows a representative comparison between the simulated and experimental data for a cutting speed of 300 m/min.

The measurement of post machining damage of MMC samples was done by obtaining SEM images. The images indicate the extent of debonding between the

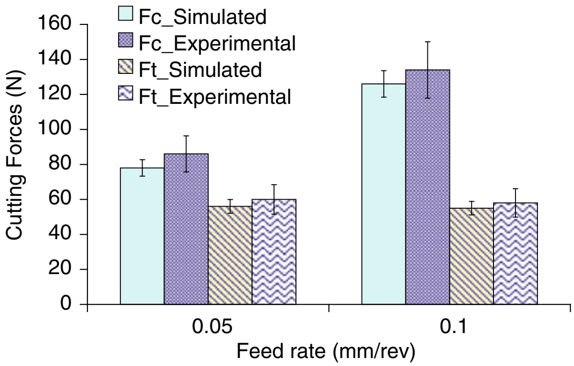

Fig. 1.24 Comparison of experimental and simulated results for cutting forces for machining at a cutting speed of 300 m/min (*source*: Dandekar and Shin [80], with permission from Elsevier)

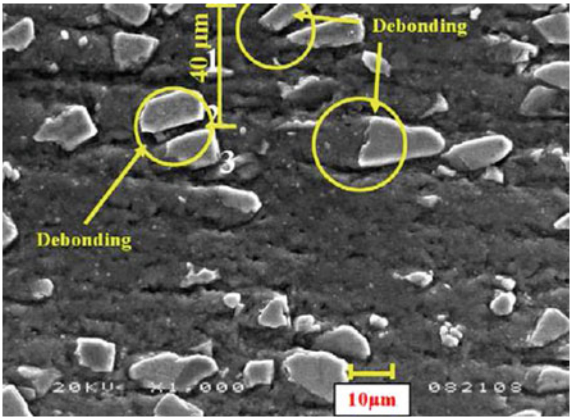

Fig. 1.25 Machined cross-section at cutting speed of 300 m/min and a feed rate of 0.05 mm/rev (*source*: Dandekar and Shin [80], with permission from Elsevier)

particles and the matrix along with particle fracture. The results indicate that the damage depth is primarily a function of feed rate. Figures 1.25 and 1.26 show the SEM images of the machined cross-section at the feed rate of 0.05 and 0.1 mm/rev at a cutting speed of 300 m/min, illustrating average sub-surface damage at 46 and 76 μm, respectively. As observed from the images it is clear that at the feed rate of 0.1 mm/rev there is a presence of higher damage, which corresponds to the higher-cutting forces observed during machining at higher feed rates. Regions of particle fracture can also be identified while machining at 300 m/min as marked on Fig. 1.26. Similar results were obtained from the SEM images for a cutting speed of 150 m/min at feed rates of 0.05 and 0.1 mm/rev, where the average sub-surface damage depth was 36 and 68 μm, respectively. As with the case of machining at 300 m/min the maximum damage was observed for a feed rate of 0.1 mm/rev.

Representative sectioned images of the simulated 100 μm cubic local damage model are shown in Figs. 1.27 and 1.28 for feed rates of 0.05 and 0.1 mm/rev, respectively at a cutting speed of 300 m/min, where the simulated von Mises stress distribution in MPa is shown. The regions of debonding and particle fracture are shown as insets of the regions where debonding and particle fracture occurred in Figs. 1.27 and 1.28. Similar simulation results were obtained for the cutting speed of

Fig. 1.26 Machined cross-section at cutting speed of 300 m/min and a feed rate of 0.1 mm/rev (*source*: Dandekar and Shin [80], with permission from Elsevier)

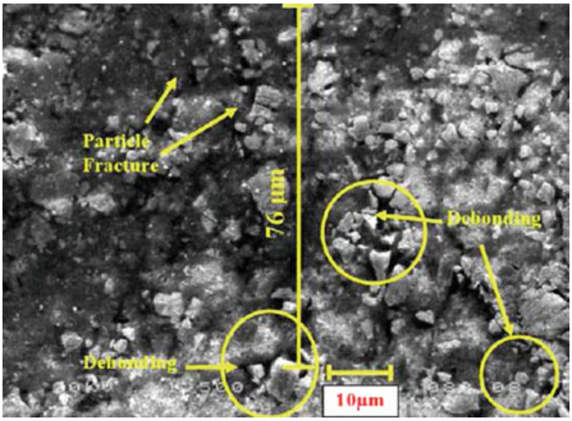

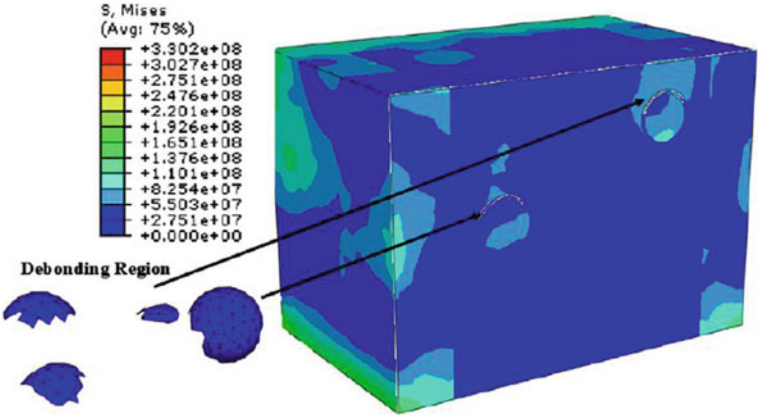

Fig. 1.27 Damage observed to a depth of 40.7 microns for a cutting speed of 300 m/min and a feed rate of 0.05 mm/rev (*source*: Dandekar and Shin [80], with permission from Elsevier)

150 m/min. Overall the experimental measurements compared very well with the simulated results, although the simulated values were slightly lower for all cases. This was consistent with the force comparisons where the thrust force was under predicted by the simulations. At a cutting speed of 150 m/min the simulated and experimental damage depths are 32 and 36 μm, respectively, for a feed rate of 0.05 mm/rev, while for a feed rate of 0.1 mm/rev the simulated and experimental measurements are 63 and 68 μm, respectively. At a cutting speed of 300 m/min and a feed rate of 0.05 and 0.1 mm/rev the simulated damage depths are 40.7 and 72 μm, respectively as shown in Figs. 1.27 and 1.28, while experimentally measured damage depths are 46 and 76 μm for a feed rate of 0.05 and 0.1 mm/rev, respectively.

During machining higher-cutting forces create more damage in terms of particle fracture and an increase in the debonding depth. This phenomenon is due to the

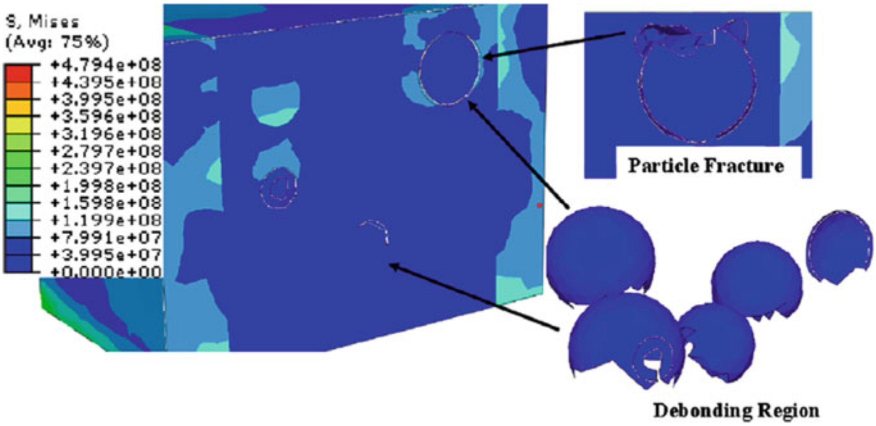

Fig. 1.28 Damage observed to a depth of 72 microns for a cutting speed of 300 m/min and a feed rate of 0.1 mm/rev (*source*: Dandekar and Shin [80], with permission from Elsevier)

interaction between the matrix and the particles. In the MMC material it is seen that the strain in the particles is much less than that observed in the matrix due to the high difference in the modulus of elasticity of the two phases. At higher-cutting forces there is a further increase in stress along the particle-matrix interface, resulting in particle fracture and deformation occurring at the bottom of the particle as seen in Fig. 1.28.

The sub-surface damage model includes capabilities for predicting debonding, particle fracture and matrix void formation. An advantage of the model is a significant reduction of computation time due to the multi-step simulation of the machining problem. A limitation of the model however, is the use of the EHM model in predicting the cutting forces. The treatment of the composite material as a homogenous material in the 3D model ignores the interaction of the tool with the particles, therefore ignoring the fluctuations in the cutting forces observed otherwise. The interaction of the particles with the tool has been studied by Pramanik et al. [19] for 2D orthogonal modeling. The effect of the particles is implicitly included in the homogenous material. To include this interaction in 3D modeling would be redundant and, hence for simplicity in applying the 3D machining model, can be neglected without losing accuracy. Nevertheless the treatment of machining simulation as a 3D nose turning results in incorporation of the effect of the tool nose radius and damage due to machining by the primary-and secondary-cutting edges.

1.6.2 Modeling Machining of Fiber Reinforced MMC

The machining simulation models presented above are all focused on particulate reinforced MMCs and there is a lack of models describing long-fiber MMC. Most of the models developed for machining of long-fiber composites deal with fiber

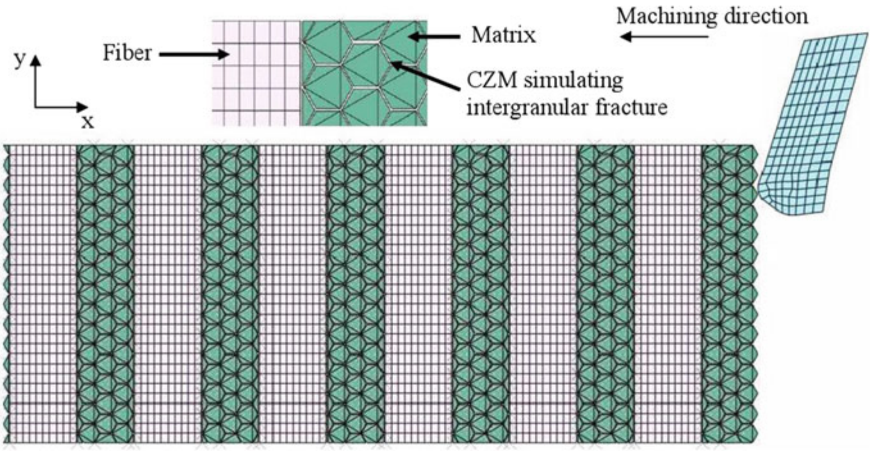

Fig. 1.29 Finite-element mesh for alumina fiber reinforced aluminum MMC (*source*: Dandekar and Shin [36], with permission from ASME)

reinforced polymer composites [72–74, 91]. All these authors indicated that the extent of damage depth and the cutting force increase with increasing fiber orientation. Utilizing a similar strategy to modeling machining of polymer composites, Dandekar and Shin [36] successfully simulated the machining of a long-fiber metal matrix composite.

In their model, a multi-phase FEM model has been implemented to study the effect of rake angle, material removal temperature and cutting speed on the machining of a long-fiber MMC [36]. The multi-phase approach utilizes a three phase finite-element mesh. The mesh is based on distinct properties of the fiber, matrix and the fiber-matrix interface and is shown in Fig. 1.29. The fiber is modeled as an anisotropic brittle material. The matrix on the other hand is considered as an elastic-plastic material modeled by a J–C model with damage in the matrix accounted for by a J–C damage model. The fiber-matrix interface and the grain boundaries are modeled using cohesive zone elements.

Simulations show that the primary method of failure in the matrix region is attributed to intergranular sliding with crack propagation achieved through failure of the cohesive zone elements. In the fiber, crack initiation and progression is accounted through the implementation of a damage law with the failure of the element resulting in the subsequent crack propagation. Figure 1.30 shows the progression of chip formation while machining of the MMC. The simulation allows the user to identify damage initiation sites, initiation of debonding at the fiber-matrix interface, fiber failure and subsequent fiber pullout. Damage in the composite after machining is characterized through excessive fiber breakage below the cutting plane. This is observed due to the brittle nature of the alumina fibers. To inspect damage after machining, SEM images were obtained by studying the interior cross-section of the workpieces. For each cutting condition, five measurements each from two different workpieces were

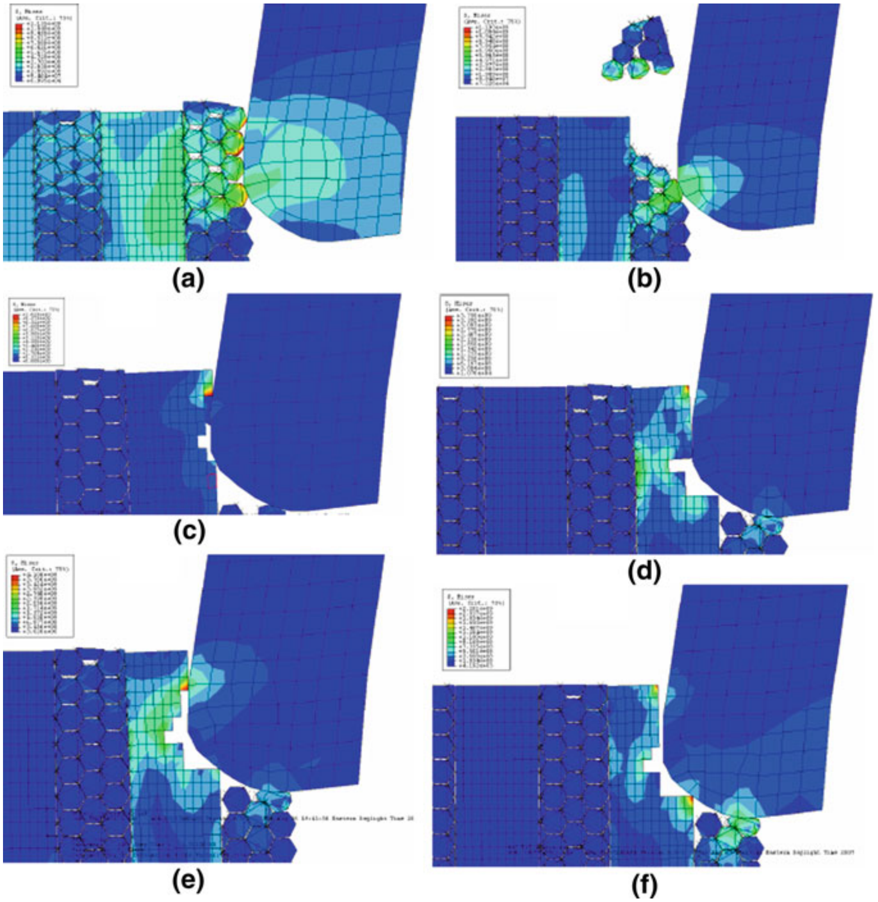

Fig. 1.30 Simulated results $Vc = 30$ m/min, $f = 0.02$ mm/rev, a tool rake angle of 5° machining of a long-fiber MMC

performed. The reported value is the average value of these 10 measurements. A variation of 20% was observed in the experimental measurements. The SEM image indicates the extent of debonding between the fiber and the matrix, microcracking of fibers and fiber pullout. The indicator for fiber pullout is the presence of matrix-rich regions after conventional machining of workpieces. The damage in the composite decreased with decreasing thrust force. A representative image for machining at a cutting speed of 30 m/min, feed of 0.02 mm/rev and depth of cut of 0.5 is shown in Fig. 1.31. A simulation result showing the fiber damage and debonding is presented in Fig. 1.32. The average measured value for the debonding/fiber damage is 157 ± 15 μm, while simulations predict a damage depth of 162 ± 2 μm. Further validations of the presented model can be obtained from Dandekar and Shin [36].

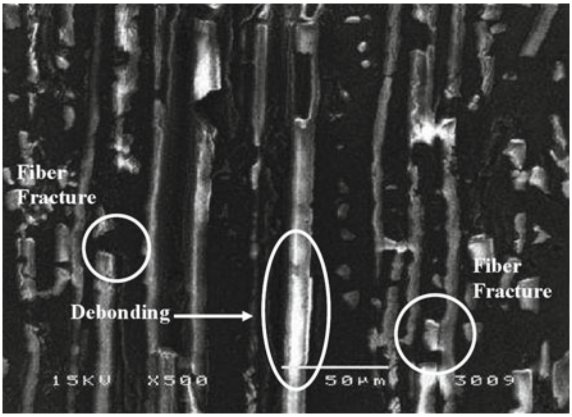

Fig. 1.31 Sub-surface damage measurement at $f = 0.02$ mm/rev $V_C = 30$ m/min, $d = 0.5$ mm for conventional machining (*source*: Dandekar and Shin [36], with permission from ASME)

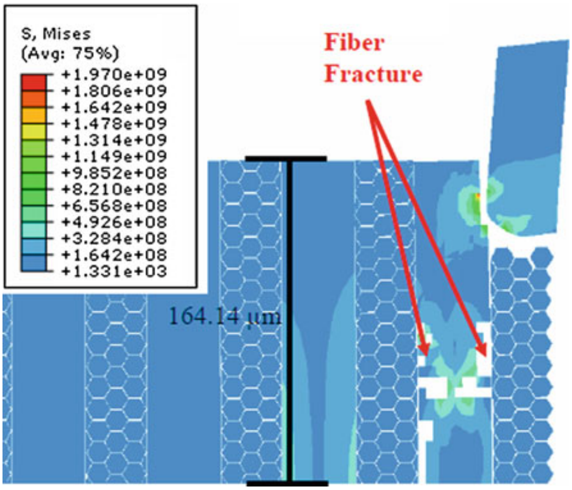

Fig. 1.32 Simulated results $Vc = 30$ m/min, $f = 0.02$ mm/rev, a tool rake angle of 5° for conventional machining (*source*: Dandekar and Shin [36], with permission from ASME)

1.7 Conclusion

In this chapter, the mechanics of chip formation in machining (turning) of particulate and fiber reinforced MMCs was introduced. Analytical models for determining the cutting forces and cutting temperatures for machining of particulate reinforced MMC’s were introduced. The cutting forces, surface quality and tool wear are mainly controlled by the reinforcement size, feed and cutting speed. Poly crystalline diamond (PCD) is the most suitable tool material for machining of MMCs. The most common chip type produced during machining of particulate MMC’s is the sawtooth type of chip. On the other hand machining of fiber reinforced composites produced chips which are extremely short and discontinuous. Most of the studies are involved with machining of particulate reinforced MMCs, while machining studies on long-fiber reinforced MMCs are highly lacking. Analytical models were presented to understand the cutting mechanism for both types of composites. The analytical models are capable of predicting the cutting forces with good accuracy, albeit they fail to account for all the various deformation phenomena observed in machining of MMCs. Analytical predictions of the cutting temperatures in machining of MMCs deviate from experimental measurements. To this end 2D and 3D finite element models were introduced to explain the chip formation process, tool–particle interaction, prediction of cutting forces, cutting temperatures and the sub-surface damage. Good agreements have been found between model predictions and experimental measurements of the cutting forces, cutting temperatures tool–chip interaction and sub-surface damage for machining of MMCs. The analytical and numerical models presented in this chapter assist in selecting machining parameters: tool geometry and cutting conditions to improve the machinability of MMC.

References

1. Weinert K, König W (1993) A consideration of tool wear mechanism when machining Metal Matrix Composites (MMC). Ann CIRP 42(1):95–98. doi:10.1016/s0007-8506(07)62400-7
2. Quigley O, Monaghan J, O'Reilly P (1994) Factors affecting the machinability of an Al/SiC metal-matrix composite. J Mater Process Tech 43(1):21–36. doi:10.1016/0924-0136(94)90159-7
3. Lin JT, Bhattacharyya D, Lane C (1995) Machinability of a silicon carbide reinforced aluminium metal matrix composite. Wear 181–183(Part 2):883–888. doi:10.1016/0043-1648(95)90211-2
4. El-Gallab M, Sklad M (1998) Machining of Al/SiC particulate metal-matrix composites. Part I: Tool performance. J Mater Process Tech 83(1–3):151–158. doi:10.1016/s0924-0136(98)00054-5
5. Andrewes CJE, Feng H-Y, Lau WM (2000) Machining of an aluminum/SiC composite using diamond inserts. J Mater Process Tech 102(1–3):25–29. doi:10.1016/s0924-0136(00)00425-8
6. El-Gallab M, Sklad M (2000) Machining of Al/SiC particulate metal matrix composites. Part III: Comprehensive tool wear models. J Mater Process Tech 101(1–3):10–20. doi:10.1016/s0924-0136(99)00351-9
7. Quan Y, Zhou Z (2000) Tool wear and its mechanism for cutting SiC particle-reinforced aluminium matrix composites. J Mater Process Tech 100(1–3):194–199. doi:10.1016/s0924-0136(99)00405-7
8. El-Gallab M, Sklad M (1998) Machining of Al/SiC particulate metal matrix composites. Part II: Workpiece surface integrity. J Mater Process Tech 83(1–3):277–285. doi:10.1016/s0924-0136(98)00072-7
9. Manna A, Bhattacharayya B (2003) A study on machinability of Al/SiC-MMC. J Mater Process Tech 140(1–3):711–716. doi:10.1016/s0924-0136(03)00905-1
10. Pramanik A, Zhang LC, Arsecularatne JA (2008) Machining of metal matrix composites: effect of ceramic particles on residual stress, surface roughness and chip formation. Int J Mach Tool Manu 48(15):1613–1625. doi:10.1016/j.ijmachtools.2008.07.008
11. Manna A, Bhattacharyya B (2004) Investigation for optimal parametric combination for achieving better surface finish during turning of Al/SiC-MMC. Int J Adv Manuf Tech 23:658–665. doi:10.1007/s00170-003-1624-z

12. Ozben T, Kilickap E, ÇakIr O (2008) Investigation of mechanical and machinability properties of SiC particle reinforced Al-MMC. J Mater Process Tech 198(1–3):220–225. doi:10.1016/j.jmatprotec.2007.06.082
13. Wang J, Huang CZ, Song WG (2003) The effect of tool flank wear on the orthogonal cutting process and its practical implications. J Mater Process Tech 142(2):338–346. doi:10.1016/s0924-0136(03)00604-6
14. Manna A, Bhattacharayya B (2005) Influence of machining parameters on the machinability of particulate reinforced Al/SiC-MMC. Int J Adv Manuf Tech 25:850–856. doi:10.1007/s00170-003-1917-2
15. Kannan S, Kishawy HA, Balazinski M (2006) Flank wear progression during machining metal matrix composites. J Manuf Sci E-T ASME 128:787–791. doi:10.1115/1.2164508
16. Muthukrishnan N, Murugan M, Prahlada Rao K (2008) Machinability issues in turning of Al-SiC (10 p) metal matrix composites. Int J Adv Manuf Tech 39:211–218. doi:10.1007/s00170-007-1220-8
17. Davim JP (2002) Diamond tool performance in machining metal-matrix composites. J Mater Process Tech 128(1–3):100–105. doi:10.1016/s0924-0136(02)00431-4
18. Joshi SS, Ramakrishnan N, Nagarwalla HE, Ramakrishnan P (1999) Wear of rotary carbide tools in machining of Al/SiCp composites. Wear 230(2):124–132. doi:10.1016/s0043-1648(99)00092-7
19. Pramanik A, Zhang LC, Arsecularatne JA (2007) An FEM investigation into the behaviour of metal matrix composites: tool-particle interaction during orthogonal cutting. Int J Mach Tool Manu 47(10):1497–1506. doi:10.1016/j.ijmachtools.2006.12.004
20. Kishawy HA, Kannan S, Balazinski M (2004) An energy based analytical force model for orthogonal cutting of metal matrix composites. Ann CIRP 53(1):91–94. doi:10.1016/s0007-8506(07)60652-0
21. Davim JP (2003) Design of optimisation of cutting parameters for turning metal matrix composites based on the orthogonal arrays. J Mater Process Tech 132(1–3):340–344. doi:10.1016/s0924-0136(02)00946-9
22. Monaghan J, Brazil D (1997) Modeling the sub-surface damage associated with the machining of a particle reinforced MMC. Comp Mater Sci 9(1–2):99–107. doi:10.1016/s0927-0256(97)00063-3
23. El-Gallab MS, Sklad MP (2004) Machining of aluminum/silicon carbide particulate metal matrix composites. Part IV: Residual stresses in the machined workpiece. J Mater Process Tech 152(1):23–34. doi:10.1016/j.jmatprotec.2004.01.061
24. Davim JP, Baptista AM (2000) Relationship between cutting force and PCD cutting tool wear in machining silicon carbide reinforced aluminum. J Mater Process Tech 103(3):417–423. doi:10.1016/s0924-0136(00)00495-7
25. Chambers AR (1996) The machinability of light alloy MMCs. Composites Part A-Appl S 27(2):143–147. doi:10.1016/1359-835x(95)00001-i
26. Ciftci I, Turker M, Seker U (2004) Evaluation of tool wear when machining SiCp-reinforced Al-2014 alloy matrix composites. Mater Des 25(3):251–255. doi:10.1016/j.matdes.2003.09.019
27. Ding X, Liew WYH, Liu XD (2005) Evaluation of machining performance of MMC with PCBN and PCD tools. Wear 259(7–12):1225–1234. doi:10.1016/j.wear.2005.02.094
28. Tomac N, Tannessen K, Rasch FO (1992) Machinability of particulate aluminium matrix composites. Ann CIRP 41(1):55–58. doi:10.1016/s0007-8506(07)61151-2
29. Arsecularatne JA, Zhang LC, Montross C (2006) Wear and tool life of tungsten carbide, PCBN and PCD cutting tools. Int J Mach Tool Manu 46(5):482–491. doi:10.1016/j.ijmachtools.2005.07.015
30. Hung NP, Zhong CH (1996) Cumulative tool wear in machining metal matrix composites. Part I: Modelling. J Mater Process Tech 58(1):109–113. doi:10.1016/0924-0136(95)02114-0
31. Heath PJ (2001) Developments in applications of PCD tooling. J Mater Process Tech 116(1):31–38. doi:10.1016/s0924-0136(01)00837-8

32. Hyde AR (1990) Ceramic matrix composites. Mater Des 11(1):30–36. doi:10.1016/0261-3069(90)90087-z
33. Komanduri R (1997) Machining of fiber-reinforced composites. Mach Sci Technol 1:113–152
34. Varadarajan YS, Vijayaraghavan L, Krishnamurthy R (2002) The machinability characteristics of aluminosilicate fiber reinforced Al alloy composite. Mater Manuf Process 17:811–824. doi:10.1081/AMP-120016059
35. Weinert K, Lange M (2003) Machining of fibre reinforced magnesium. In: Proceedings of the second Osaka international conference on platform science and technology for advanced magnesium alloys 2003, Jan 26, 2003–Jan 30, 2003, Osaka, Japan. Materials science forum. Trans Tech Publications Ltd, pp 823–828
36. Dandekar CR, Shin YC (2010) Laser-assisted machining of a fiber reinforced metal matrix composite. J Manuf Sci E-T ASME 132(6):061004–061008. doi:10.1115/1.4002548
37. Davim JP (2007) Application of merchant theory in machining particulate metal matrix composites. Mater Des 28(10):2684–2687. doi:10.1016/j.matdes.2006.10.015
38. Merchant ME (1945) Mechanics of the metal cutting process. I. Orthogonal cutting and a type 2 chip. J Appl Phys 16:267–275
39. Waldorf DJ (2006) A simplified model for ploughing forces in turning. J Manuf Processes 8:76–82
40. Yan C, Zhang L (1994) Single-point scratching of 6061 Al alloy reinforced by different ceramic particles. Appl Compos Mater 1:431–447
41. Zhang LC (2009) Cutting composites: a discussion on mechanics modelling. J Mater Process Tech 209(9):4548–4552. doi:10.1016/j.jmatprotec.2008.10.023
42. Boothroyd G, Knight WA (2005) Fundamentals of machining and machine tools. crc mechanical engineering, 3rd edn. CRC Pr I Llc, Boca Raton, Florida
43. Liu J, Chou YK (2007) Cutting tool temperature analysis in heat-pipe assisted composite machining. J Manuf Sci E-T ASME 129:902–910. doi:10.1115/1.2752528
44. Weiner JH (1955) Shear-plane temperature distribution in orthogonal cutting. T ASME 77(8):1331–1336
45. Rapier AC (1954) A theoretical investigation of the temperature distribution in the metal cutting process. Brit J Appl Phys 5(11):400–405. doi:10.1088/0508-3443/5/11/306
46. Kalpakjian S (1996) Manufacturing processes for engineering materials. Addison-Wesley, Reading, MA
47. Karthikeyan R, Ganesan G, Nagarazan RS, Pai BC (2001) A critical study on machining of Al/SiC composites. Mater Manuf Process 16:47–60. doi:10.1081/AMP-100103696
48. Monaghan J, Brazil D (1998) Modelling the flow processes of a particle reinforced metal matrix composite during machining. Composites Part A-Appl S 29(1–2):87–99. doi:10.1016/s1359-835x(97)00047-x
49. Hung NP, Yeo SH, Lee KK, Ng KJ (1998) Chip formation in machining particle-reinforced metal matrix composites. Mater Manuf Process 13:85–100
50. Hung NP, Loh NL, Venkatesh VC (1999) Machining of metal matrix composites. In: Jahanmir S, Ramulu M, Koshy P (eds) Machining of ceramics and composites. Marcel Dekker Inc, New York, pp 295–356
51. Joshi SS, Ramakrishnan N, Ramakrishnan P (2001) Micro-structural analysis of chip formation during orthogonal machining of Al/SiCp composites. J Eng Mater-T ASME 123:315–321. doi:10.1115/1.1356026
52. Koplev A, Lystrup A, Vorm T (1983) The cutting process, chips, and cutting forces in machining CFRP. Composites 14(4):371–376. doi:10.1016/0010-4361(83)90157-x
53. Takeyama H, Iijima N (1988) Machinability of glassfiber reinforced plastics and application of ultrasonic machining. Ann CIRP 37(1):93–96. doi:10.1016/s0007-8506(07)61593-5
54. Kim KS, Lee DG, Kwak YK, Namgung S (1992) Machinability of carbon fiber-epoxy composite materials in turning. J Mater Process Tech 32(3):553–570. doi:10.1016/0924-0136(92)90253-o

55. Nayak D, Bhatnagar N, Mahajan P (2005) Machining studies of uni-directional glass fiber reinforced plastic (UD-GFRP) composites. Part 1: Effect of geometrical and process parameters. Mach Sci Technol 9:481–501. doi:10.1080/10910340500398167
56. Wang XM, Zhang LC (1999) Machining damage in unidirectional fiber-reinforced plastics. In: Wan J, Scott W, Zhang LC (eds) Abrasive technology—current development and applications. World Scientific, Singapore, pp 429–436
57. Zhang LC, Zhang HJ, Wang XM (2001) A force prediction model for cutting unidirectional fibre-reinforced plastics. Mach Sci Technol 5:293–305. doi:10.1081/MST-100108616
58. Bergman F, Jacobson S (1994) Tool wear mechanisms in intermittent cutting of metal matrix composites. Wear 179(1–2):89–93. doi:10.1016/0043-1648(94)90224-0
59. Mackerle J (1998) Finite-element analysis and simulation of machining: a bibliography (1976–1996). J Mater Process Tech 86(1–3):17–44. doi:10.1016/s0924-0136(98)00227-1
60. Mackerle J (2003) Finite element analysis and simulation of machining: an addendum: a bibliography (1996–2002). Int J Mach Tool Manu 43(1):103–114. doi:10.1016/s0890-6955(02)00162-1
61. Soo SL, Aspinwall DK (2007) Developments in modeling of metal cutting processes. In: IMechE, vol. 221, Part L: J Mater Design Appl, pp 197–211
62. ABAQUS User's Manual, Version 6.5 (2004) Hibbitt, Karlsson & Sorensen, Inc., Pawtucket, RI
63. Olovsson L, Nilsson L, Simonsson K (1999) An ALE formulation for the solution of two-dimensional metal cutting problems. Comput Struct 72(4–5):497–507. doi:10.1016/s0045-7949(98)00332-0
64. Movahhedy MR, Altintas Y, Gadala MS (2002) Numerical analysis of metal cutting with chamfered and blunt tools. J Manuf Sci E-T ASME 124:178–188. doi:10.1115/1.1445147
65. Movahhedy M, Gadala MS, Altintas Y (2000) Simulation of the orthogonal metal cutting process using an arbitrary Lagrangian-Eulerian finite-element method. J Mater Process Tech 103(2):267–275. doi:10.1016/s0924-0136(00)00480-5
66. Tian Y, Shin YC (2004) Finite element modeling of machining of 1020 steel including the effects of round cutting edge. In: Papers Presented at NAMRC 32, June 1, 2004–June 4, 2004, Charlotte, NC, United states, Transactions of the North American Manufacturing Research Institute of SME. Society of Manufacturing Engineers, pp 111–118
67. Özel T, Zeren E (2005) Finite element method simulation of machining of AISI 1045 Steel with a Round Edge Cutting Tool. In: Proceedings of 8th CIRP international workshop on modeling of machining operations. Chemnitz, Germany
68. Ozel T, Zeren E (2007) Finite element modeling the influence of edge roundness on the stress and temperature fields induced by high-speed machining. Int J Adv Manuf Tech 35:255–267. doi:10.1007/s00170-006-0720-2
69. Haglund AJ, Kishawy HA, Rogers RJ (2008) An exploration of friction models for the chip-tool interface using an Arbitrary Lagrangian-Eulerian finite element model. Wear 265(3–4):452–460. doi:10.1016/j.wear.2007.11.025
70. Dandekar CR, Shin YC, Barnes J (2010) Machinability improvement of titanium alloy (Ti-6Al-4 V) via LAM and hybrid machining. Int J Mach Tools Manuf 50(2):174–182. doi: 10.1016/j.ijmachtools.2009.10.013
71. Camus G (2000) Modelling of the mechanical behavior and damage processes of fibrous ceramic matrix composites: application to a 2D SiC/SiC. Int J Solids Struct 37(6):919–942. doi:10.1016/s0020-7683(99)00065-7
72. Arola D, Ramulu M (1997) Orthogonal cutting of fiber-reinforced composites: a finite element analysis. Int J Mech Sci 39(5):597–613. doi:10.1016/s0020-7403(96)00061-6
73. Arola D, Sultan MB, Ramulu M (2002) Finite element modeling of edge trimming fiber reinforced plastics. J Manuf Sci E-T ASME 124:32–41
74. Nayak D, Bhatnagar N, Mahajan P (2005) Machining studies of ud-frp composites. Part 2: Finite element analysis. Mach Sci Technol 9:503–528. doi:10.1080/10910340500398183

75. Rao GVG, Mahajan P, Bhatnagar N (2007) Machining of UD-GFRP composites chip formation mechanism. Compos Sci Technol 67(11–12):2271–2281. doi:10.1016/j.compscitech.2007.01.025
76. Rao GVG, Mahajan P, Bhatnagar N (2007) Micro-mechanical modeling of machining of FRP composites—cutting force analysis. Compos Sci Technol 67(3–4):579–593. doi:10.1016/j.compscitech.2006.08.010
77. Johnson GR, Cook WH (1983) A constitutive model and data for metals subjected to large strains, high rates and high temperatures. In: Proceedings of the seventh international symposium on ballistics. The Hague, the Netherlands, pp 541–547
78. Norton FH (1929) Creep of steel at high temperature. McGraw-Hill, New York
79. HOFF NJ (1954) Approximate analysis of structures in the presence of moderately large creep deformations. Q Appl Math 12:49–55
80. Dandekar CR, Shin YC (2009) Multi-step 3D finite element modeling of subsurface damage in machining particulate reinforced metal matrix composites. Composites Part A: Appl Sci Manuf 40(8):1231–1239. doi:10.1016/j.compositesa.2009.05.017
81. Zhou L, Huang ST, Wang D, Yu XL (2011) Finite element and experimental studies of the cutting process of SiCp/Al composites with PCD tools. Int J Adv Manuf Tech 52:619–626. doi:10.1007/s00170-010-2776-2
82. Macdougall DAS, Harding J (1999) A constitutive relation and failure criterion for Ti6Al4 V alloy at impact rates of strain. J Mech Phys Solids 47(5):1157–1185. doi:10.1016/s0022-5096(98)00086-6
83. Follansbee PS, Gray GT III (1989) An analysis of the low temperature, low and high strain-rate deformation of Ti-6Al-4 V. Metall Trans A 20A:863–874
84. Nemat-Nasser S, Guo W-G, Nesterenko VF, Indrakanti SS, Gu Y-B (2001) Dynamic response of conventional and hot isostatically pressed Ti-6Al-4 V alloys: experiments and modeling. Mech Mater 33:425–439. doi:10.1016/S0167-6636(01)00063-1
85. Lemaitre J, Desmorat R (2005) Engineering damage mechanics: ductile, creep, fatigue and brittle failures. Springer-Verlag, Berlin, Heidelberg
86. Marusich TD, Ortiz M (1995) Simulation of chip formation in high-speed machining. In: Proceedings of the 1995 joint ASME applied mechanics and materials conference, Machining of Advanced Materials, AMD, pp 127–139
87. Cantonwine PE (2003) Strength of thermally exposed alumina fibers. Part I: Single filament behavior. J Mater Sci 38:461–470. doi:10.1023/A:1021867530979
88. 3M (2004) Nextel^{TM} Ceramic textilestechnical notebook. St. Paul, MN
89. Bansal NP (2005) Handbook of ceramic composites. Kluwer Academic Publishers, New York
90. Orifici AC, Herszberg I, Thomson RS (2008) Review of methodologies for composite material modelling incorporating failure. Comput Struct 86(1–3):194–210. doi:10.1016/j.compstruct.2008.03.007
91. Dandekar CR, Shin YC (2008) Multiphase finite element modeling of machining unidirectional composites: prediction of debonding and fiber damage. J Manuf Sci E-T ASME 130:0510161–05101612. doi:10.1115/1.2976146
92. Needleman A (1987) A continuum model for void nucleation by inclusion debonding. J Appl Mech-T ASME 54:525–531
93. Tvergaard V (1990) Effect of fibre debonding in a whisker-reinforced metal. Mater Sci Eng 125(2):203–213. doi:10.1016/0921-5093(90)90170-8
94. Xu XP, Needleman A (1995) Numerical simulations of dynamic crack growth along an interface. Int J Fracture 74:289–324
95. Camacho GT, Ortiz M (1996) Computational modelling of impact damage in brittle materials. Int J Solids Struct 33(20–22):2899–2938. doi:10.1016/0020-7683(95)00255-3
96. Chandra N, Li H, Shet C, Ghonem H (2002) Some issues in the application of cohesive zone models for metal-ceramic interfaces. Int J Solids Struct 39(10):2827–2855. doi:10.1016/s0020-7683(02)00149-x

97. Xie JQ, Bayoumi AE, Zbib HM (1998) FEA modeling and simulation of shear localized chip formation in metal cutting. Int J Mach Tool Manu 38(9):1067–1087. doi:10.1016/s0890-6955(97)00063-1
98. Bäker M, Rösler J, Siemers C (2002) A finite element model of high speed metal cutting with adiabatic shearing. Comput Struct 80(5–6):495–513. doi:10.1016/s0045-7949(02)00023-8
99. Simoneau A, Ng E, Elbestawi MA (2006) Chip formation during microscale cutting of a medium carbon steel. Int J Mach Tool Manu 46(5):467–481. doi:10.1016/j.ijmachtools.2005.07.019
100. Shet C, Deng X (2000) Finite element analysis of the orthogonal metal cutting process. J Mater Process Tech 105(1–2):95–109. doi:10.1016/s0924-0136(00)00595-1
101. Ceretti E, Lucchi M, Altan T (1999) FEM simulation of orthogonal cutting: serrated chip formation. J Mater Process Tech 95(1–3):17–26. doi:10.1016/s0924-0136(99)00261-7
102. Hua J, Shivpuri R (2002) Influence of crack mechanics on the chip segmentation in the machining of Ti-6Al-4 V. In: Proceedings of the 9th ISPE international conference on concurrent engineering, Cranfield, UK, pp 357–365
103. Filice L, Micari F, Rizzuti S, Umbrello D (2007) A critical analysis on the friction modelling in orthogonal machining. Int J Mach Tool Manu 47(3–4):709–714. doi:10.1016/j.ijmachtools.2006.05.007
104. Zhu Y, Kishawy HA (2005) Influence of alumina particles on the mechanics of machining metal matrix composites. Int J Mach Tool Manu 45(4–5):389–398. doi:10.1016/j.ijmachtools.2004.09.013
105. Quan Y, Ye B (2003) The effect of machining on the surface properties of SiC/Al composites. J Mater Process Tech 138(1–3):464–467. doi:10.1016/s0924-0136(03)00119-5
106. Reddy PR, Sriramakrishna AA (2002) Analysis of orthogonal cutting of aluminum-based composites. Defence Sci J 52(4):375–382
107. Chou YK, Liu J (2005) CVD diamond tool performance in metal matrix composite machining. Surf Coat Tech 200(5–6):1872–1878. doi:10.1016/j.surfcoat.2005.08.094
108. Rintoul MD, Torquato S (1997) Reconstruction of the structure of dispersions. J Colloid Interf Sci 186(2):467–476. doi:10.1006/jcis.1996.4675